Contents lists available at ScienceDirect

Bioactive Materials

journal homepage: www.keaipublishing.com/en/journals/bioactive-materials

Exosome-functionalized magnesium-organic framework-based scaffolds with osteogenic, angiogenic and anti-inflammatory properties for accelerated bone regeneration

Yue Kang [a], Chang Xu [b], Ling'ao Meng [a], Xufeng Dong [b], Min Qi [b], Daqing Jiang [a],*

[a] Department of Breast Surgery, Cancer Hospital of China Medical University, 44 Xiaoheyan Road, Dadong District, Shenyang, 110042, PR China
[b] School of Materials Science and Engineering, Dalian University of Technology, 2 Linggong Road, Ganjingzi District, Dalian, 116024, China

ARTICLE INFO

ABSTRACT

Exosomes derived from human adipose-derived stem cells (hADSCs-Exos) have shown potential as an effective therapeutic tool for repairing bone defects. Although metal-organic framework (MOF) scaffolds are promising strategies for bone tissue regeneration, their potential use for exosome loading remains unexplored. In this study, motivated by the potential advantages of hADSCs-Exos and Mg-GA MOF, we designed and synthesized an exosome-functionalized cell-free PLGA/Mg-GA MOF (PLGA/Exo-Mg-GA MOF) scaffold, taking using of the benefits of hADSCs-Exos, Mg^{2+}, and gallic acid (GA) to construct unique nanostructural interfaces to enhance osteogenic, angiogenic and anti-inflammatory capabilities simultaneously. Our *in vitro* work demonstrated the beneficial effects of PLGA/Exo-Mg-GA MOF composite scaffolds on the osteogenic effects in human bone marrow-derived mesenchymal stem cells (hBMSCs) and angiogenic effects in human umbilical endothelial cells (HUVECs). Slowly released hADSCs-Exos from composite scaffolds were phagocytosed by co-cultured cells, stabilized the bone graft environment, ensured blood supply, promoted osteogenic differentiation, and accelerated bone reconstruction. Furthermore, our *in vivo* experiments with rat calvarial defect model showed that PLGA/Exo-Mg-GA MOF scaffolds promoted new bone formation and satisfactory osseointegration. Overall, we provide valuable new insights for designing exosome-coated nanocomposite scaffolds with enhanced osteogenesis property.

1. Introduction

The regeneration of bone defects caused by trauma, infection, tumors or inherent genetic disorders is a global clinical challenge. Every year more than 10 million bone graft procedures are performed, with the rate still growing at 10% per year [1]. Despite the self-healing capability of bone, larger bone defects are preferentially treated with autologous bone grafting, however, limited bone supply and donor site morbidity are major disadvantages of this approach [2]. Similarly, allogenic bone grafting exhibits poor stability, significant failure rates, and carries a risk of graft-versus-host disease due to immunological rejection [3]. Therefore, these strategies are not optimal treatment options for bone regeneration.

Bone tissue engineering (BTE) is a rapidly developing area for repairing large bone defects [4]. BTE-construction relies on three essential components: innovative scaffolds, seed cells, and osteoinductive factors [5]. However, the implantation of seed cells, such as hADSCs, faces significant challenges, including immune rejection [6], teratoma formation [7] and undirected cell differentiation [8]. Therefore, bone regeneration without externally seeded stem cells, termed cell-free regeneration, is a promising solution for these cell-derived problems [9]. Indeed, the implantation of cell-free scaffolds for cell-free bone tissue regeneration [10] has emerged as a prospective approach to avoid these issues.

To achieve cell-free tissue regeneration, cell-free scaffolds should contain effective osteoinductive factors, such as BMP-2 and BMP-9. However, increasing side effects are reported during the clinical use of osteoinductive factors, such as ectopic bone formation, inflammation,

bone resorption, and hematoma [11]. Thus, demand for effective, alternative osteoinductive factors is driven by the severe side effects of existing drugs. One such highly promising osteoinductive factor for regenerative medicine are exosomes; they are naturally secreted vesicles (40–150 nm) with lipid-bilayers encapsulating proteins, lipids, genetic information, and metabolites, which facilitate intercellular communications [12]. Exosomes secreted by human adipose-derived mesenchymal stem cells (hADSCs-Exos) are reportedly superior in enhancing the efficacy of biomaterials for bone regeneration [13]. In addition, hADSCs-Exos exhibit immunomodulatory functions and create a beneficial bone immune microenvironment for osteogenesis [14]. When compared with existing drugs or mesenchymal stem cells (MSCs), MSC-derived exosomes generate distinct advantages and reduce side effects, such as improved stability, limited immune rejection, convenient administration, and easy internalization into recipient cells [15]. Based on these characteristics, and previous studies [16,17] reporting the pro-angiogenic effects of hADSCs-derived exosomes, these reagents appear to be ideal osteoinductive factors in "cell-free" tissue engineering strategies.

Metal-organic frameworks (MOFs) are constructed from metal ion/cluster nodes and functional organic ligands via coordination bonds [18], and are promising platforms for biomedical applications due to unique combinations of structural diversity, high surface areas, adjustable porosity, simple surface functionalization, and tunable biocompatibility [19,20]. The application of MOF incorporated scaffolds is a promising strategy for bone tissue regeneration, e.g., ZIF-8-modified multifunctional bone-adhesive hydrogels promoted angiogenesis and osteogenesis during bone regeneration [21]. Also, Cooper et al. reported that a biocompatible porous Mg-gallate Metal Organic Framework, its slow degradation in physiological fluids leads to the release of GA and Mg^{2+} [22]. Mg^{2+} are the most abundant divalent cations in cells, regulating multiple cellular functions, including cell signaling, cell growth, metabolism, and proliferation [23]. Studies have reported that Mg^{2+}, which are formed by biodegradation, promote the osteogenic differentiation of MSCs by elevating autophagic activities [24]. Thus, appropriate Mg^{2+} concentrations activate calcium ion channels on cell membranes and promote calcium deposition which is essential for bone growth [25]. In addition, the angiogenic [26] and anti-inflammatory [27] activities of Mg^{2+} provide additional protection in various bone regeneration conditions. Therefore, these molecules are excellent bone formation factors and underpin the wide use of Mg bone tissue engineering materials for bone repair. GA and its derivatives are a group of polyphenol compounds with potent antioxidative and anti-inflammatory abilities [28]. It is accepted that osteogenic differentiation is restored by attenuating inflammation [29], therefore, GA could play key roles in bone formation. While studies on MOFs for drug delivery have rapidly increased [30–32], their potential application for exosome loading remains largely unexplored.

Poly (lactic acid-co-glycolic acid) (PLGA) has been employed for implantable devices based on their unique biocompatibility, tunable biodegradability, acceptable mechanical properties, and FDA approval [33]. Electrospun PLGA fibers are capable of stimulating cell-matrix interaction to form a cell niche, directing cellular behavior, and promoting the MSCs adhesion and proliferation [34,35]. In this work, we integrate exosomes from human MSCs with cell-free PLGA/Mg-GA MOF nanofibrous scaffolds to construct functional biomaterial scaffolds for bone-tissue regeneration. We expect that PLGA/Mg-GA MOF scaffolds coated with exosomes extracted from hADSCs could released Mg^{2+}, GA, and exosomes slowly to enhance anti-inflammatory abilities, osteogenic differentiation, and angiogenesis for accelerated bone regeneration. The relevant properties of PLGA/Mg-GA MOF scaffolds were investigated, and biological performance of exosome-coated PLGA/Mg-GA MOF scaffolds was characterized comprehensively the *in vitro* and *in vivo*.

2. Experimental section

2.1. Cell culture, stimulation, and characterization

Human ADSCs, hBMSCs, human umbilical endothelial cells (HUVECs) and RAW264.7 mouse macrophages (leukemia cells in a mouse macrophage cell line) were used in this study. Human BMSCs were obtained from Otwo Biotech Inc. (Catalog no. HTX1946, China). HUVECs were obtained from Otwo (Catalog no. HTX1922). RAW264.7 cells were obtained from Otwo (Catalog no. HTX1760). HUVECs were cultured in a high-glucose Dulbecco's Modified Eagle's Medium (DMEM, HyClone, UT, USA) supplemented with the 10% fetal bovine serum (FBS, HyClone, UT, USA) and 1% penicillin/streptomycin (Gibco, NY, USA). Human ADSCs, hBMSCs, and RAW264.7 cells were cultured in Dulbecco's Modified Eagle Medium (DMEM) (HyClone, UT, USA), 10% fetal bovine serum (FBS), and 1% penicillin-streptomycin (Gibco, NY, USA) in a 5% CO_2 humidified atmosphere at 37 °C. The culture medium was replaced every two days.

For osteogenic differentiation, the hBMSCs (1×10^4 cells/scaffold) were stimulated with 10% FBS supplemented with osteogenic components: 2 mM β-glycerophosphate, 1 mL 0.1 mmol/L L-ascorbic acid 2-phosphate, and 10 μL 10^{-8} mol/L dexamethasone; (Cyagen, Guangzhou,China).

Multi-lineage potential assays and flow cytometry analyses were performed to identify hADSC characteristics, as described previously [36]. Antibodies, including anti-CD34-FITC, anti-CD45-PE, anti-CD90-PE, anti-CD73-PE, and anti-CD105-PE were purchased from BD Biosciences (CA, USA).

2.2. Isolation and characterization of exosomes

Human ADSCs (passage 3) were seeded in culture medium at 1×10^6 cells. When cells reached 75% confluence, the medium was replaced with serum-free DMEM at 37 °C for 48 h prior to the collection of the conditioned medium (CM). Cells were counted at time of CM harvesting, and cell viability was >95% (trypan blue staining). CM was cleared by three sequential centrifugation steps at $300 \times g$ (10 min), $2000 \times g$ (20 min) and $10,000 \times g$ (30 min), followed by filtration with 0.45 and 0.22 μm filters. A subsequent ultra-centrifugation at $100,000 \times g$ for 70 min yielded a raw exosome extract, which was washed with PBS once, followed by another ultracentrifugation at $\times$ g for 70 min. The resulting precipitate contained pure exosomes, which were suspended in an appropriate volume of PBS. Exosomes were further purified by sucrose cushion depending on the experimental usage (Fig. S1). The Micro BCA Protein Assay Kit (Thermo Fisher Scientific, MA, USA) was used to analyze exosome release; protein concentrations of collected exosomes were measured at days 1, 4, 7, 10, and 13.

The morphology of exosomes was observed and recorded by transmission electron microscope (TEM, JEM-F200, JEOL). First, 10 μL of obtained exosomes were added to the copper net to form water droplets and the excess liquid was absorbed before drying. During dyeing, 10 μL of uranium acetate was added and dyed for 30s in dark. The concentration and particle size distribution were measured by nanoparticle tracking analysis (NTA, Nanosight NS300, Malvern). In short, 1 mL of exosome suspension was carefully transferred to a syringe. And the zeta potential was measured by Zetasizer Nano ZS90 (Malvern). 1 mL of exosome solution was filtered with a 0.22 μm sterile filter for zeta potential testing.

The characteristic markers including TSG101, Calnexin, CD63 and CD81 were analyzed by Western blot, as described in Western Blotting Analysis.

2.3. Materials and methods

Magnesium chloride, gallic acid and 1,1,1,3,3,3-hexafluoro-2-propanol (HFIP, 99.5%) were purchased from Macklin (Shanghai, China).

Table 1
Composition for PLGA/Mg-GA MOF scaffolds.

Composition	Mg-GA MOF(mg)	PLGA(mg)	Mg-GA MOF/PLGA(w/w)
PLGA/Mg-GA$_1$	170	1700	10%
PLGA/Mg-GA$_2$	255	1700	15%
PLGA/Mg-GA$_3$	340	1700	20%

Poly (D,L-lactide-co-glycolide) (LA:GA = 75:25, MW = 80,000) was purchased from Jinan Daigang (Jinan, China). KOH was purchased from Sinopharm Chemical Reagent (Shanghai, China).

The morphology and surface characteristics were characterized under a NOVA NanoSEM 450 Field Emission Scanning Electron Microscope (FESEM, FEI, USA), the chemical composition was recorded by attenuated total reflection-fourier transform infrared spectra (ART-FTIR, ThermoFisher, USA), the X-ray diffraction (XRD) patterns were obtained from SmartLab 9 KW X-ray diffractometer (Rigaku, Japan). The thermal stability of the scaffolds was obtained by thermogravimetric analysis (TGA, Mettler Toledo, Switzerland) and the hydrophilicity was obtained through a water contact angle tester (WCA, Kruss, Germany). The concentration of magnesium ions released from the scaffolds were measured by inductively coupled plasma atomic emission spectrometer (ICP-AES, Perkinelmer, USA). The Brunauer−Emmett−-Teller (BET) method was utilized to evaluate the surface area and porosity measurements, and performed on a Autosorb iQ analyzer (Quantachrome, USA).

2.4. Preparation of Mg-GA MOF

Biocompatible and non-toxic Mg-based MOF was synthesized using a hydrothermal method [22]. Briefly, 1 g MgCl$_2$ was dissolved in 50 mL ultrapure water (18.2 MΩ, Millipore Co., USA), to which 3.8 g GA was added. A large, milky white precipitation was produced and stirred vigorously for 30 min. Then, a 10 M aqueous solution of potassium hydroxide was added drop-wise to adjust to pH 8. The precipitation gradually disappeared and the milky white solution gradually turned to brownish-yellow. After stirring for 10 min, the solution was moved to a 100 mL autoclave and autoclaved at 120 °C for 24 h. The solution was cooled to room temperature, centrifuged at 10000 rpm for 10 min, and the supernatant discarded. The light grey solid pellet was washed three times in ultrapure water and dried in an oven at 60 °C overnight.

2.5. Preparation of PLGA/Mg-GA MOF composite scaffolds and exosome-coated PLGA/Mg-GA MOF scaffolds

We used electrospinning technology [37] to prepare composite scaffolds. A 6.5 mm diameter scaffold was used for in vitro and in vivo studies (Fig. S10). Briefly, PLGA was dissolved in HFIP and stirred overnight to generate a 15% (w/v) electrospinning solution. Then, various quantities of Mg-GA MOF (10%, 15%, and 20% w/w of PLGA) were added, and the MOF dispersed evenly by ultrasound and stirring. Electrospinning parameters were: 15–17 kV in voltage; 0.8–1.0 mL/h for flow rate of the electrospinning solution. Electrospinning was performed at room temperature. Then, fiber membranes were collected on aluminum foil and dried for 24 h at 30 °C.

Hereafter, the PLGA/Mg-GA MOF composite scaffold will be termed PLGA/Mg-GA, and divided into PLGA/Mg-GA$_1$, PLGA/Mg-GA$_2$, and PLGA/Mg-GA$_3$ according to different mass ratios, from low Mg-GA MOF composition to high, respectively (Table 1). The PLGA alone served as a control-group.

To immobilize hADSCs-Exos, the prescribed quantity was suspended in 1 mL PBS (pH 7), added to composite scaffolds, and incubated overnight at 4 °C. The hADSCs-Exos immobilized onto scaffolds were determined by measuring protein concentrations in PBS solutions before and after binding reactions. The amount of hADSCs-Exos (40 μg/mL, Fig. S8) added was slightly lower than the maximal loading capacity of

the PLGA/Mg-GA$_2$ to ensure the full binding of exosomes in the solution.

2.6. Exosome labeling and internalization

Human ADSCs-Exos were labeled with PKH26 (Sigma-Aldrich, MO, USA) according to manufacturer's instructions. Briefly, purified hADSCs-Exos were incubated in 4 μL PKH26 for 5 min, and the reaction stopped by adding an equal volume of 1% bovine serum albumin. Labeled exosomes were then ultracentrifuged at $100000 \times g$ for 120 min, washed in PBS, and re-ultracentrifuged. Finally, labeled exosomes were resuspended in PBS prior to use.

Recipient cells (hBMSCs or RAW264.7) were cultured with PKH26-labeled exosomes for 12 h, followed by 4% paraformaldehyde fixation for 20 min. After washing three times in PBS, the nuclei were stained with 4′,6′-diaminido-2-phenylindole (DAPI, Thermo Fisher, MA, USA) at room temperature for 5 min. Exosome uptake into recipient cells was observed using fluorescence microscopy (Olympus, Japan).

2.7. Scaffold biocompatibility

2.7.1. Cell morphology

Approximately 1×10^4 hBMSCs/mL were seeded onto scaffolds (Fig. 3B) using a bespoke instrument designed for seeding cells onto scaffolds for 72 h. Then, samples were rinsed twice in PBS and fixed in 4% paraformaldehyde at room temperature for 15 min. Samples were then permeabilized in 0.5% Triton X-100 for 5 min, washed three times in PBS, and stained with FITC-phalloidin (ab235137, Abcam, UK) for 30 min, and DAPI for a further 5 min in the dark. FITC-phalloidin (red) and nuclei (blue) on scaffolds were examined using fluorescence microscopy (Olympus, Japan).

2.7.2. Cell proliferation

We seeded hBMSCs on scaffolds (n = 6) at 1×10^4 cells/mL. Cell proliferation was investigated using a cell counting kit-8 (CCK-8, Dojindo, Japan) after 1, 3, 5, and 7 days of culturing. At these time points, cells were rinsed twice in PBS, and fresh medium (300 μL) and CCK-8 solution (30 μL) added to wells, followed by incubation at 37 °C for 2 h. Then, 100 μL of the supernatant was transferred to a 96-well plate and, we measured the absorbance at 450 nm to detect proliferation of cells.

2.7.3. Live/dead double staining

We seeded hBMSCs on scaffolds at 1×10^4 cells/mL and incubated them for 24 h. Cell cytotoxicity on scaffolds was detected using a live/dead double-staining kit (KeyGen, China). Cells were stained with 2 μM calcein-AM and 8 μM propidium iodide (PI) for 15 min. Live cells were green by calcein-AM staining, whereas dead cells were red from PI staining. Stained specimens were observed and imaged using fluorescence microscopy (Leica, Germany).

2.8. Assessment of angiogenic effects

HUVECs were used to analyze the in-vitro cell angiogenesis. The PLGA, PLGA/Mg-GA$_2$, and PLGA/Exo-Mg-GA$_2$ scaffolds were immersed for 72 h for preparing extracts according to ISO 10993-12. Three kinds of extracts including PLGA, PLGA/Mg-GA$_2$, and PLGA/Exo-Mg-GA$_2$ for the following wound healing assay, transwell migration assay, and tube formation assay were collected without any filtration. HUVECs without additional treatment was used as the control group.

For wound healing assay, HUVECs were seeded in a 6-well plate as a monolayer. A sterile 200-μl pipette tip was used to scratch a straight line. The three kinds of extracts were applied. Images were obtained at 24 h and analyzed. The results were derived from three repeated experiments.

For transwell assay, 1.0×10^5 HUVECs were seeded in the upper chamber of transwell 24-well plates (8 μm pore size, Corning Costar,

USA). 800 μL of diluted extract mentioned above was added to the lower chamber per well. After 24 h, the cells in the upper chamber were removed by a cotton swab, and the cells on the membrane were stained with Hematoxylin and eosin staining (H&E, Beyotime, China). The results were analyzed by Image J software.

For tube formation assay, HUVECs were pretreated with the diluted extract for 24 h. The cells were harvested and seeded at a density of 5×10^4 cells/well on Matrigel (Corning Costar, USA) in 24-well plates. The original culture medium was subsequently replaced by the diluted extract mentioned above. After 6 h' co-culturing, the tube structures formed in the gel were photographed in a microscope. The tube formation parameters were measured by Image J software.

2.9. Alkaline phosphatase staining and Alizarin red S staining

A 5-bromo-4-chloro-3-indolyl phosphate/nitro blue tetrazolium (BCIP/NBT) ALP color development kit (Beyotime) was used to stain the ALP activity of hBMSCs. After hBMSCs were fixed in 4% paraformaldehyde for 30 min, pre-prepared BCIP/NBT dyeing was added and incubated with samples for 1 h to stain ALP. BCIP/NBT dyeing was removed and rinsed by distilled water to terminate the staining reaction. The images of ALP staining were captured by a digital camera (Canon) and microscopy (Olympus).

ARS staining was used to measure the property of mineralized nodule formation. Briefly, BMSCs were fixed in 75% ethanol for 1 h. Afterward, 2% ARS solution (pH 4.2, Sigma–Aldrich) was dripped onto the samples and incubated for 10 min. Unreacted ARS was rinsed thoroughly using distilled water. The images of deposited calcium were captured by a digital camera (Canon) and microscopy (Olympus).

2.10. Anti-inflammatory abilities of scaffolds

To assess the anti-inflammatory abilities of the different scaffolds, RAW264.7 (1×10^4 cells/well) were seeded on the scaffolds as the previous method, following 10% FBS incubated for 24 h, and then stimulated with lipopolysaccharide (LPS, 1 μg/mL, Sigma-Aldrich, USA) for 24 h, the group without a scaffold as the positive control. Finally, the cells were collected to analyze Cyclooxygenase-2 (COX-2) and inducible nitric oxide synthase (iNOS) expression by western blotting.

2.11. Western blotting

Cells were lysed in RIPA buffer (Beyotime Biotech., China), and extracted proteins were quantified using a bicinchoninic acid protein assay kit (Beyotime). Proteins were separated using 11% sodium dodecyl sulfate-polyacrylamide electrophoresis, transferred to polyvinylidene fluoride membranes (Millipore, USA) and stained in Ponceau S (Beyotime) for 10 min. Then, membranes were blocked in 5% skim milk in Tris Buffered Saline + Tween (TBST) at room temperature for 45 min. After washing in TBST, membranes were incubated with primary antibodies overnight at 4 °C. After washing and incubating with secondary antibodies, protein bands were detected using chemiluminescence (ECL) (Solarbio, China). β-actin was used as a loading control. The primary antibodies used in the present study were listed in Table S1.

2.12. Immunofluorescence staining

Immunofluorescence was used to identify human ALP, Runx2, OCN, and VEGF proteins. After fixation and permeabilization, hBMSCs were incubated with primary antibodies in humid conditions overnight at 4 °C. After washing in PBS, corresponding secondary antibodies were added to the primary antibodies for 1 h. The primary antibodies used in the present study were listed in Table S1. After washing in PBS, cells were incubated with DAPI for 10 min to delineate nuclei. Immunofluorescence images were captured using fluorescence microscopy (Leica,

Germany).

2.13. In vivo animal studies

2.13.1. Critical-size calvarial bone defect model

All animal studies were approved by the Animal Care and Use Committee of China Medical University (IACUC-2020012). Six-week old male Sprague Dawley (SD) rats (weighing 250–300 g) were anesthetized using 2% pentobarbital intraperitoneal injection. Then, a midline sagittal incision was made through the scalp skin and the subcutaneous and periosteum tissue parted to expose the calvarium. Using cooled sterile saline, a 6.5 mm bone defect on the calvarium was created using a trephine drill. A scaffold of diameter 6.5 mm and height 1.0 mm was implanted at the defect site and the skin wound sutured. Animals were sacrificed at 10 weeks post-surgery. The whole cranium plus scaffold was harvested and fixed in 4% paraformaldehyde for histological analyses. The 18 rats were divided into three groups (n = 6); PLGA/Mg-GA$_2$, PLGA/Exo-Mg-GA$_2$, and a blank group (without any scaffold).

2.13.2. Micro-computed tomography (CT) analysis

Bone regeneration in rat calvarial defect areas was evaluated and visualized using micro-computed tomography (micro-CT) (Skyscan, Kontich, Belgium) at 5 and 10 weeks post-surgery. Bone mineral density (BMD) rates and bone volume/total volume (BV/TV) were examined using CT. An software (Bruker Micro-CT, USA). Three-dimension (3D) rat calvarial micro-CT images were obtained using CTvox software (Bruker Micro-CT).

2.13.3. Histology and immunohistochemistry (IHC)

All samples were decalcified in 15% ethylenediaminetetraacetic acid (EDTA, pH 7.2) and refreshed every 3 days for 4 weeks. After dehydrated using a tissue processor, samples were embedded in paraffin, and cut into serial 5-μm sections (Leica, Germany) for staining. The pathological sections of each group were evaluated by Hematoxylin and eosin staining (H&E, Beyotime, China), Masson's trichrome staining, and images were captured with a light optical microscope (Olympus, Japan).

To perform immunohistochemistry (IHC) staining, deparaffinized samples were stained with ALP, Runx2, OCN, VEGF and CD31. The primary antibodies used in the present study were listed in Table S2. The secondary antibodies were treated for 1 h at room temperature. After secondary antibody treatment, sections were washed three times with PBS, and then labeled using AB reagent (Vector, USA) for 30 min to couple with DAB. Tissue sections were counterstained with hematoxylin and then mounted using mounting medium. Stained tissue images were obtained by digital pathology scanner (Pannoramic 250 FLASH III, 3D Histech, Hungary). The expression of IHC stained sections were measured using Image J program (IHC profiler).

2.14. Statistical analysis

SPSS 21.0 (NY, USA) and GraphPad Prism 7 (Version 7.02) (CA, USA) were used for statistical analyses. All data were expressed as the mean ± standard deviations (SD, n = 3) and processed using Student t tests. A $p < 0.05$ was considered statistically significant.

3. Results and discussion

3.1. Human ADSCs express MSC-specific markers and undergo multi-lineage differentiation

Human ADSCs are considered seed cells from tissue-engineered bone, with a broad application base [36]. Similarly, they exhibit significant advantages in terms of strong proliferation, differentiation characteristics, uniform immunophenotypes, and importantly, no ethical issues [38]. Thus, hADSCs are an attractive source of MSCs for regenerative medicine. In this study, we selected adipose tissue as a
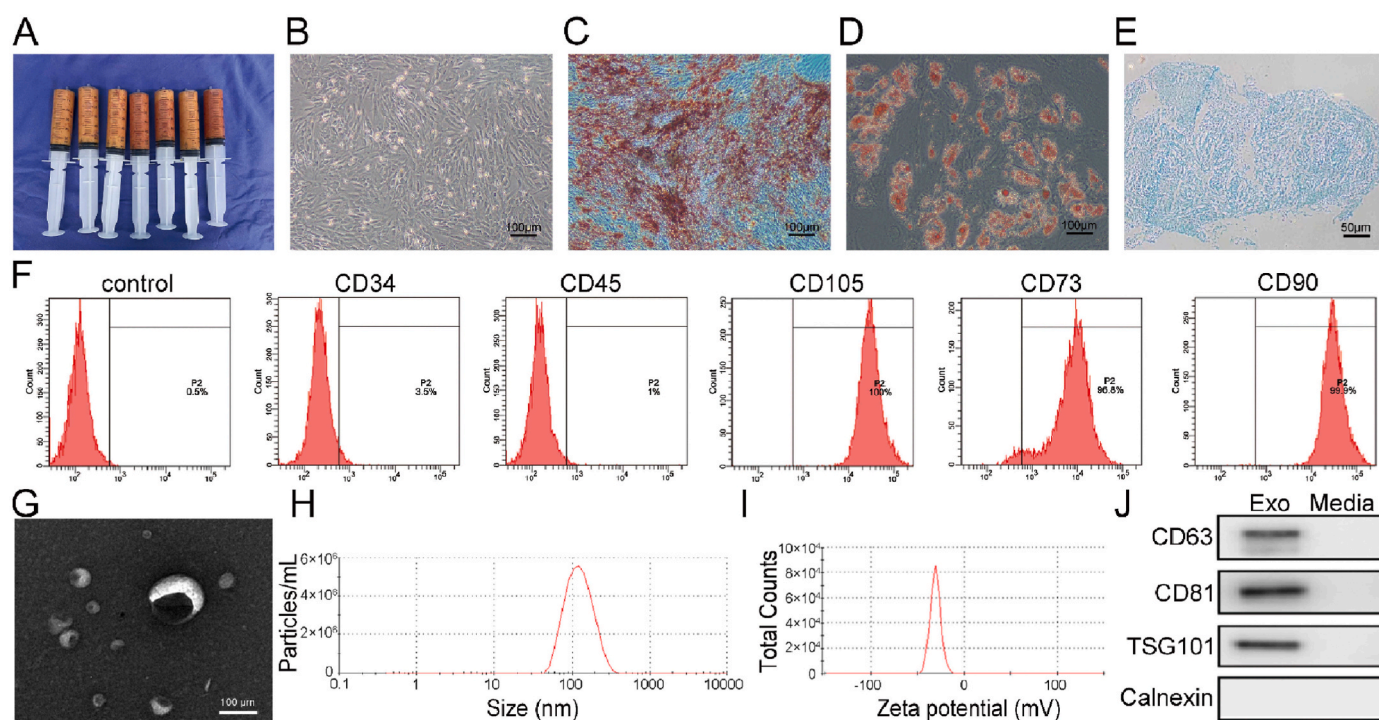
Fig. 1. Human ADSC and hADSCs-Exos characteristics. (A) Human adipose tissue was obtained by liposuction aspiration. **(B)** Representative photomicrographs of hADSC morphological characteristics. **(C)** Osteogenesis is represented by orange-red mineralized nodule formation after osteogenic induction (Alizarin Red staining). **(D)** Adipogenesis is shown by red lipid droplets in the cytoplasm after adipogenic induction (Oil Red O staining). **(E)** Chondrogenesis is indicated by round, multilayered cells with blue nuclei and cytoplasm after chondrogenic induction (Alcian Blue solution). **(F)** Flow cytometry showing positive and negative hADSC surface markers. **(G)** Exosome size and morphology by TEM. Scale bar: 50 nm. **(H)** Size distribution measurement of exosomes using the particle size & zeta potential analyzer. **(I)** Evaluation of zeta potential in exosomes. **(J)** Specific exosome markers by western blotting.

source of exosomes. Human adipose tissue (Fig. 1A) was obtained by liposuction aspiration and it was processed as previously described [39, 40]. All protocols for human tissue collection and handling were approved by the Research Ethics Committee of the Cancer Hospital of China Medical University (Approval no: 2020G0328). hADSCs that we used in this study were obtained by collagenase digestion from these adipose tissue. Fig. 1B showed the cultured hADSCs morphology evaluated by optical microscopy. To identify hADSC characteristics, multi-lineage potential assays and flow cytometry analyses were performed. As shown (Fig. 1C–E), hADSCs differentiated into adipocytes, osteoblasts, and chondrocytes in each respective induction culture medium. Also, CD34 and CD45 were negatively expressed in hADSCs, whereas CD105, CD73, and CD90 were positively expressed (Fig. 1F). These findings confirmed differentiation capacities and phenotypes of hADSCs, in agreement with the literature [41].

### 3.2. Analysis of exosomes extracted from hADSCs

Transmission electron microscopy (TEM) observations showed that vesicles of particle sizes 40 nm–150 nm appeared as discs, indicating exosomes (Fig. 1G). The nanoparticle tracking analysis (NTA) data showed that the main peak distributed at 128.2 ± 3.2 nm (Fig. 1H), and the peak particle zeta potential was -30.7 ± 1.1 mV (Fig. 1I). Additionally, western blotting confirmed that hADSCs-Exos highly expressed the exosomal protein markers, CD63, CD81, and TSG101, but not the exosomal-negative protein marker, calnexin (Fig. 1J). These results demonstrated the successful extraction of hADSCs-derived exosomes.

3.3. Fabrication and characterization of PLGA/Mg-GA MOF scaffolds

Mg-GA MOF and PLGA/Mg-GA MOF scaffolds were synthesized as shown (Fig. 2A). The successful synthesis of Mg-GA MOF was further

demonstrated by X-ray diffraction (XRD) and the routine XRD pattern were shown in Fig. 2B, which was consistent with previous reports [42, 43]. The crystallinity of Mg-GA MOF was calculated to be 6.96 (0.07)% (Fig. S3). Then, we used Fourier Transform InfraRed (FT-IR) spectrum analysis to characterize chemical bonds and interactions between Mg and GA (Fig. S4). The absorption peaks between 3493 cm^{-1} and 3284 cm^{-1} were due to stretching vibrations of multiple –OH molecules in the structure. In the characteristic region, the 1542 cm^{-1} peak was attributed to the backbone vibration peak of the benzene ring, 1027 cm^{-1} originated from the in-plane bending vibration of the benzene ring, and the peak at 1342 cm^{-1} indicated the carboxylate. For Mg-GA MOF, the spectra showed characteristic peaks at 1398 and 1546 cm^{-1} which originated from the symmetric and asymmetric stretching C–O of carboxylic acid group (OCO-) vibrations. The peak at 1702 cm^{-1} of the pure GA spectrum corresponded to the carbonyl group, while it disappeared in Mg-GA MOF, suggesting the carbonyl group of GA was affected by Mg ion coordination. Then we characterized the surface morphology of Mg-GA MOF particles using Field Emission Scanning Electron Microscope (FESEM) (Fig. 2C), which showed that the size and shape of MOF particles were irregular.

Thus, PLGA/Mg-GA MOF composite scaffolds were prepared using electrospinning technology and physicochemical properties evaluated. Based on our digital photographs and SEM images (Fig. 2H), all scaffold groups displayed good fibrous morphology. The surface of the PLGA scaffold was smooth and uniform, but after Mg-GA MOF addition, the fibrous membrane became rougher, and lumpy materials were observed. A high porosity is an essential prerequisite for effective bone substitute materials [44], and scaffolds with an optimal pore size facilitate bone in-growth and neovascularization [45,46]. The addition of Mg-GA MOF made the composite scaffolds suitable for use as a bone graft. According to Energy Disperse Spectroscopy (EDS) mapping and energy spectrum analysis (Figs. S5–6), Mg-GA MOF was successfully introduced and
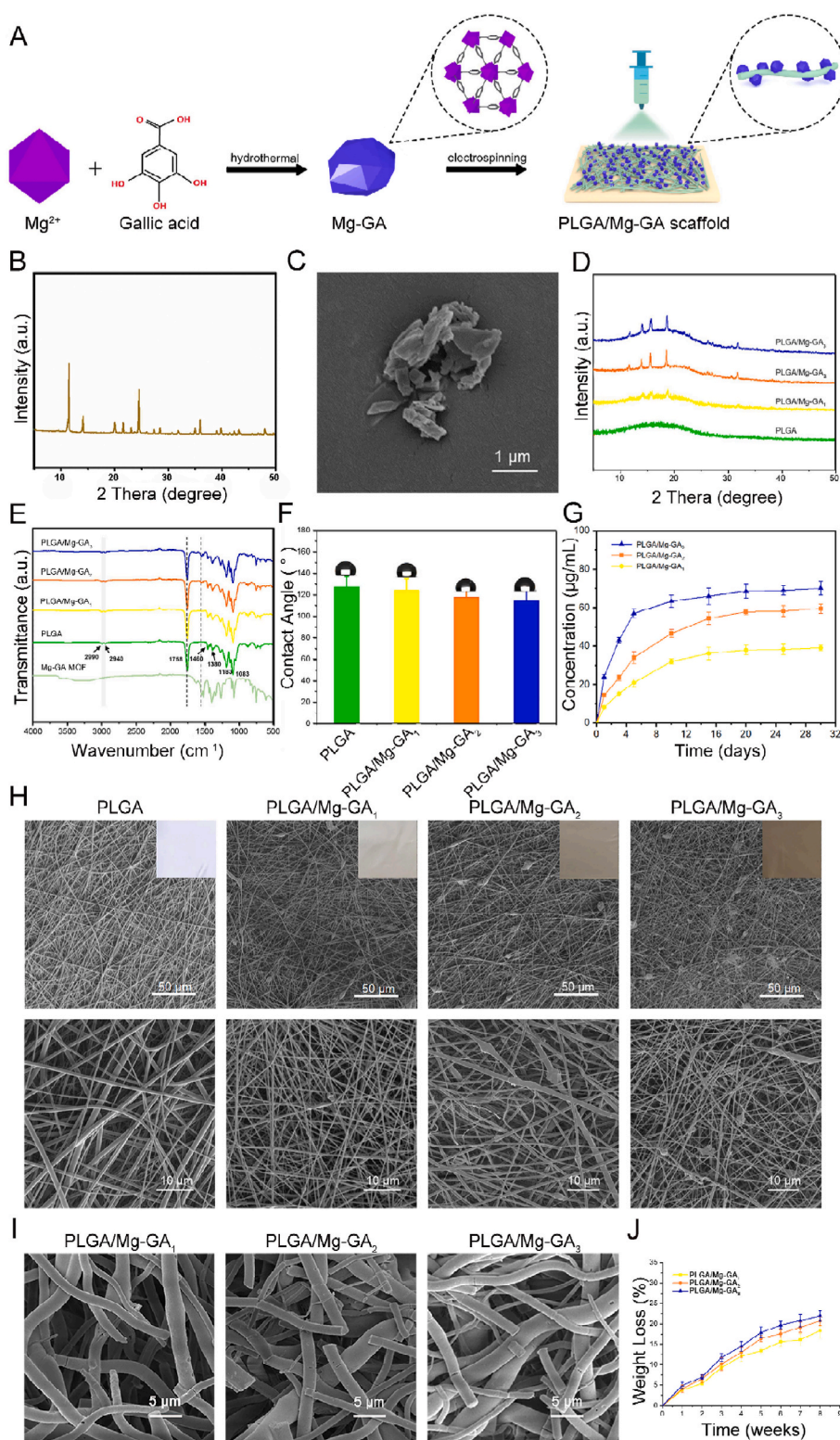
Fig. 2. Fabrication and characterization of Mg-GA MOF composite scaffolds. (A) Scheme showing Mg-GA MOF and PLGA/Mg-GA MOF scaffold preparation. **(B)** XRD spectra of Mg-GA MOF nanoparticles. **(C)** Scanning electron microscopy (SEM) images of Mg-GA MOF nanoparticles. **(D)** XRD spectra of different PLGA/Mg-GA MOF scaffolds. **(E)** FT-IR spectra of different PLGA/Mg-GA MOF scaffolds. **(F)** Contact angles of different PLGA/Mg-GA MOF scaffolds. **(G)** The release profiles of Mg^{2+} of different PLGA/Mg-GA MOF scaffolds over 1 month. **(H)** Digital photographs and SEM images of different PLGA/Mg-GA MOF scaffolds. **(I)** The biodegradability of different PLGA/Mg-GA MOF scaffolds. **(J)** The degradation curve of different PLGA/Mg-GA MOF scaffolds over 8 weeks.

uniformly distributed in the composite scaffolds. XRD patterns are shown (Fig. 2D); PLGA showed broad amorphous features with no crystalline peaks. For all three composites, crystalline phase characteristic peaks were obvious and further illustrated the incorporation of Mg-GA MOF. The chemical composition of scaffolds by FT-IR spectroscopy are shown (Fig. 2E). Pure PLGA nano-fibers showed characteristic peaks at 1083 cm^{-1} and 1183 cm^{-1} (C–O–C symmetric stretching vibration of the ester bond), 1380 cm^{-1} (-CH$_3$ stretching vibration), 1460

cm^{-1}, 2990 cm^{-1}, 2940 cm^{-1} (-CH$_2$ stretching vibrations), and 1758 cm^{-1} (C=O stretching vibration in the ester group). For composite scaffold spectra, all showed characteristic absorption peaks for PLGA and Mg-GA MOF, thereby confirming each PLGA/Mg-GA scaffold group contained a blend of parental materials. We also evaluated scaffold hydrophilicity (Fig. 2F); with increasing Mg-GA MOF quantities, contact angles gradually decreased, with a slight hydrophilicity increase. Due to the excellent biodegradability of the scaffold (Fig. 2I and J) and Mg-GA
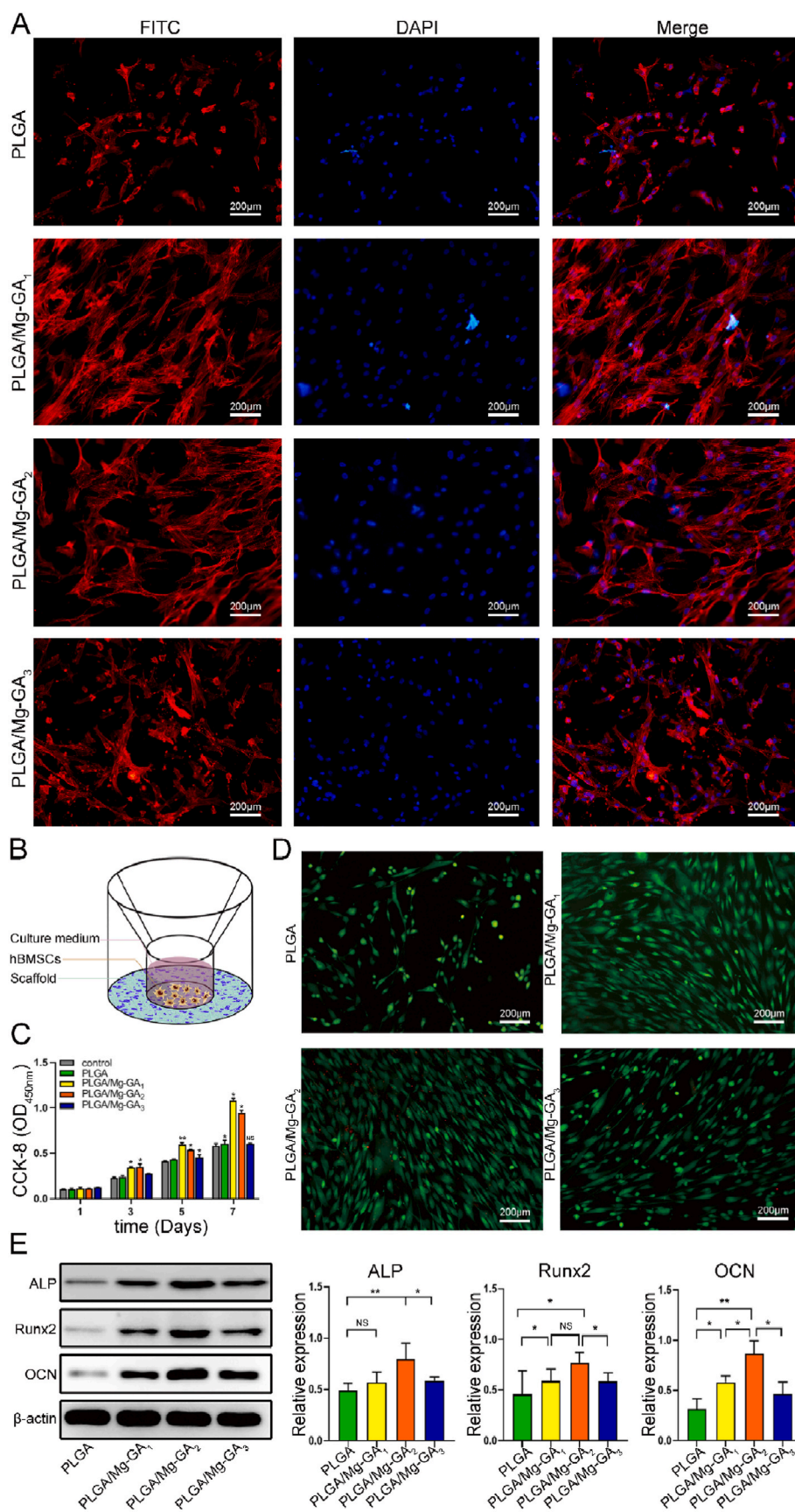
Fig. 3. *In vitro* biological properties of PLGA/Mg-GA MOF scaffolds. **(A)** Immunofluorescence images showing hBMSC morphology on different PLGA/Mg-GA MOF scaffolds. Human BMSC nuclei are stained with DAPI (blue) and the cytoskeleton stained with FITC (red). **(B)** A bespoke instrument was designed for seeding cells on scaffolds. **(C)** CCK-8 assay of hBMSCs on different scaffolds after 1, 3, 5, and 7 days. **(D)** Live/dead assay of hBMSCs cultured on scaffold surfaces for 3 days. Red staining indicates dead cells and green staining indicates live cells. **(E)** Osteogenic-related protein expression in hBMSCs on different scaffolds by western blotting. Data are presented as the mean ± standard deviation (SD) (n = 6, *P < 0.05, **P < 0.01, ***P < 0.001).
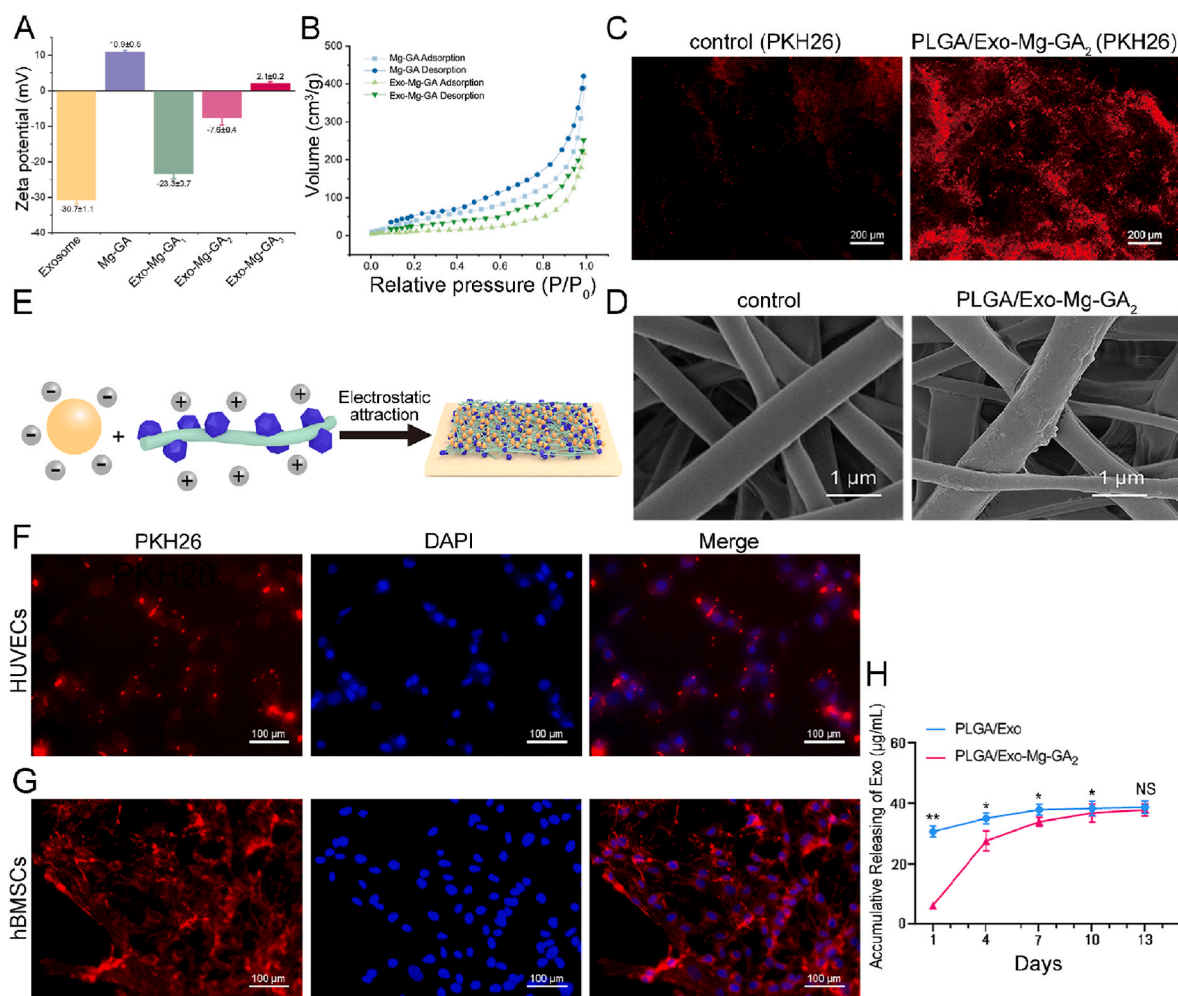
Fig. 4. Human ADSCs-Exos adhesion to PLGA/Mg-GA MOF scaffolds. (A) Zeta potential evaluation in exosomes, Mg-GA MOFs and mixtures. **(B)** The nitrogen adsorption−desorption curves of Mg-GA and Exo-Mg-GA. **(C)** The PKH26-labeled exosomes were attached obviously different to the control (PLGA) and PLGA/Mg-GA$_2$. **(D)** Scanning electron microscopy (SEM) showing nanoscale roughness on PLGA/Mg-GA$_2$ surfaces from exosome coating. **(E)** Schematic showing immobilized exosomes on PLGA/Mg-GA MOF scaffolds via electrostatic interactions. **(F)** Cellular uptake assays showing PKH26-labeled exosomes were internalized and distributed in the perinuclear region of HUVECs. HUVECs were stained with DAPI (blue) and exosomes stained with PKH26 (red). **(G)** Cellular uptake assays showing PKH26-labeled exosomes were internalized and distributed in the perinuclear region of hBMSCs. **(H)** Exosome accumulative release using the micro-BCA assay at days 1, 4, 7, 10, and 13. Data are presented as the mean ± standard deviation (SD) (n = 6, *P < 0.05, **P < 0.01).

MOF, Mg^{2+} were gradually released. The cumulative release of Mg^{2+} over 1 month was measured using inductively coupled plasma atomic emission spectrometer (ICP-AES), with release profiles shown (Fig. 2G). The cumulative release of PLGA/Mg-GA$_1$, PLGA/Mg-GA$_2$, and PLGA/Mg-GA$_3$ was 36 μg/mL, 54 μg/mL, and 65 μg/mL for the first 15 days, and up to 39 μg/mL, 59 μg/mL, and 70 μg/mL over 1 month, respectively. These observations indicated the successful preparation of PLGA/Mg-GA composite scaffolds and the slow release of Mg ions. In particular, Mg ion release from the PLGA/Mg-GA$_2$ scaffold was more stable than the others. Thus, Mg-based MOF not only exhibited nano-pores, but also released Mg ions to form a localized, high-Mg microenvironment for cell growth.

3.4. In vitro biological properties of PLGA/Mg-GA MOF scaffolds

#### 3.4.1. PLGA/Mg-GA MOF scaffold biocompatibility

Human BMSC proliferation and adhesion are fundamental properties for *in vivo* tissue reconstruction, and are widely used to characterize *in vitro* bone regeneration models [47]. Human BMSCs cultured on different composite scaffolds were evaluated for mesenchymal specific morphology, proliferative capacity, and live/dead double staining. After incubation with scaffolds for 3 days, DAPI/FITC-phalloidin fluorescence

staining indicated that hBMSCs adequately covered both PLGA/Mg-GA$_1$ and PLGA/Mg-GA$_2$ surfaces (Fig. 3A). Cells exhibited a shuttle, polygonal shape with obvious pseudopods, and also intercellular filaments were observed. We then used the CCK8 assay to evaluate hBMSC proliferation on different composite scaffolds. As shown (Fig. 3C), hBMSC proliferation on PLGA/Mg-GA$_1$ and PLGA/Mg-GA$_2$ scaffolds increased in comparison to hBMSCs on the other scaffolds. Among groups, PLGA/Mg-GA$_1$ and PLGA/Mg-GA$_2$ exhibited considerable upregulation of proliferation rate. Viability observations suggested no cytotoxic effects were generated by scaffolds, with only a few dead cells detected on surfaces (Figure.3D and Fig. S7).

3.4.2. Osteogenic differentiation of PLGA/Mg-GA MOF scaffolds

In terms of osteogenic differentiation, we explored the effects of different composite scaffolds on the expression of osteogenic proteins (Fig. 3E); ALP and Runx2 are important early stage markers in osteogenic differentiation [48,49] and OCN appears in late osteogenic differentiation periods [50]. We seeded hBMSCs on different composite scaffolds, and after 14 days culturing, the PLGA/Mg-GA$_2$ scaffold showed significantly upregulated ALP, Runx2, and OCN expression when compared with PLGA/Mg-GA$_1$, PLGA/Mg-GA$_3$, and PLGA groups. These findings demonstrated PLGA/Mg-GA$_2$ effectively promoted
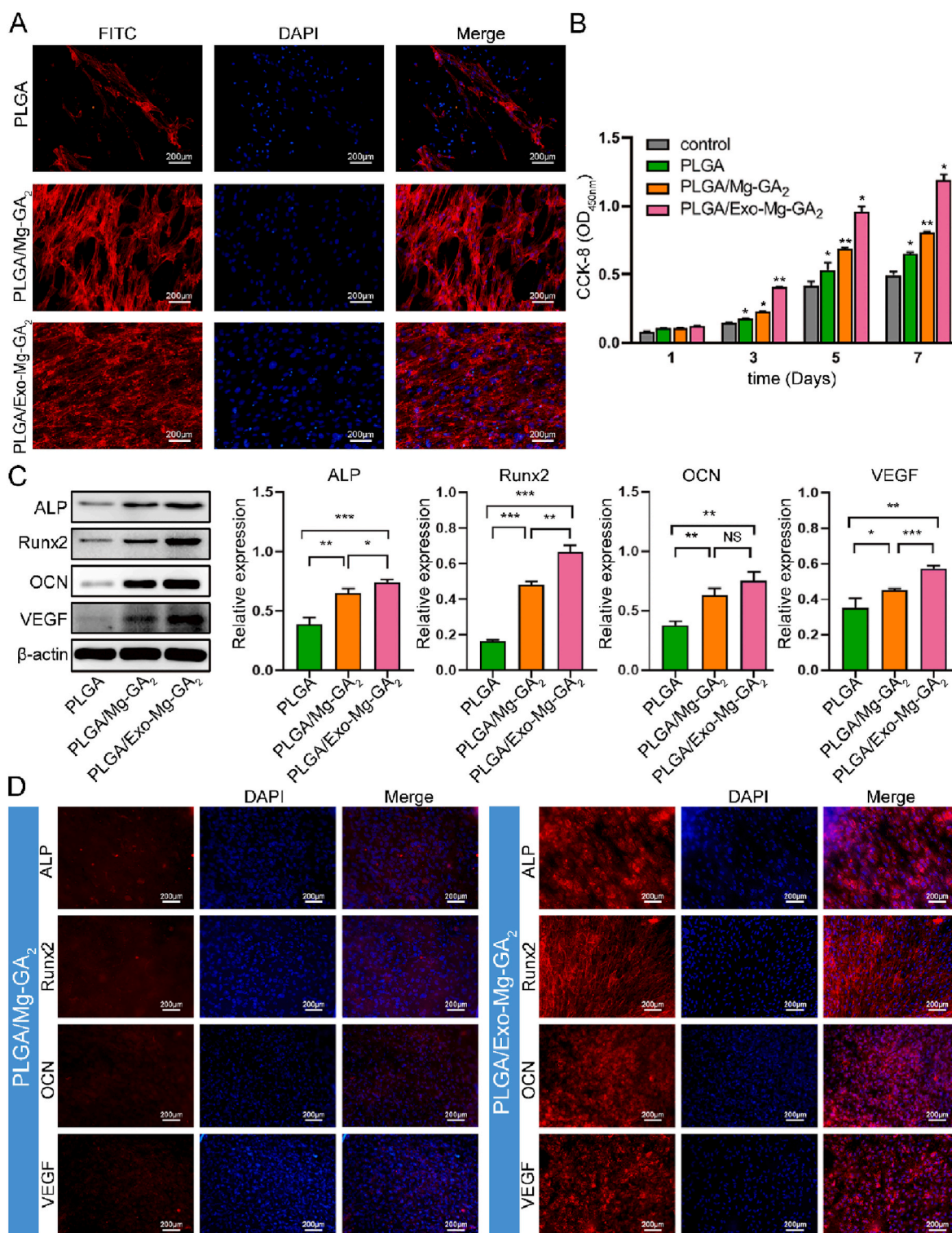
Fig. 5. *In vitro* **biological properties of exosome-coated Mg-GA MOF scaffolds. (A)** Immunofluorescence showing hBMSC morphology on PLGA/Exo-Mg-GA MOF scaffolds. Human BMSCs nuclei are stained with DAPI (blue) and cytoskeletons stained with FITC (red). **(B)** CCK-8 assay of hBMSCs on different scaffolds after 1, 3, 5, and 7 days. **(C)** Osteogenic-related and angiogenic-related protein expression in hBMSCs on PLGA/Exo-Mg-GA MOF scaffolds by western blotting. Data are presented as the mean ± standard deviation (SD) (*$P < 0.05$, **$P < 0.01$, ***$P < 0.001$). **(D)** The osteogenic markers, ALP, Runx2, and OCN and angiogenic-related marker, VEGF were positive for immunofluorescence. Cell nuclei were stained with DAPI (blue).

hBMSC osteogenic differentiation at all osteogenesis stages. Li et al. reported that with increased Mg^{2+} concentrations on material surfaces, cell adhesion and proliferation on the material showed a downward trend, after an initial increase [51]. Also, a recent study showed that Mg^{2+} at an appropriate concentration stimulated hBMSC osteogenic proliferation and differentiation [52]. In addition, it was reported that GA insertion onto chitosan markedly increased the osteogenic effects of BMSCs, the functions of which were mediated by the canonical Wnt/β-catenin signaling pathway [53]. Similarly, other studies also demonstrated that porous scaffolds allowed hBMSCs proliferate more
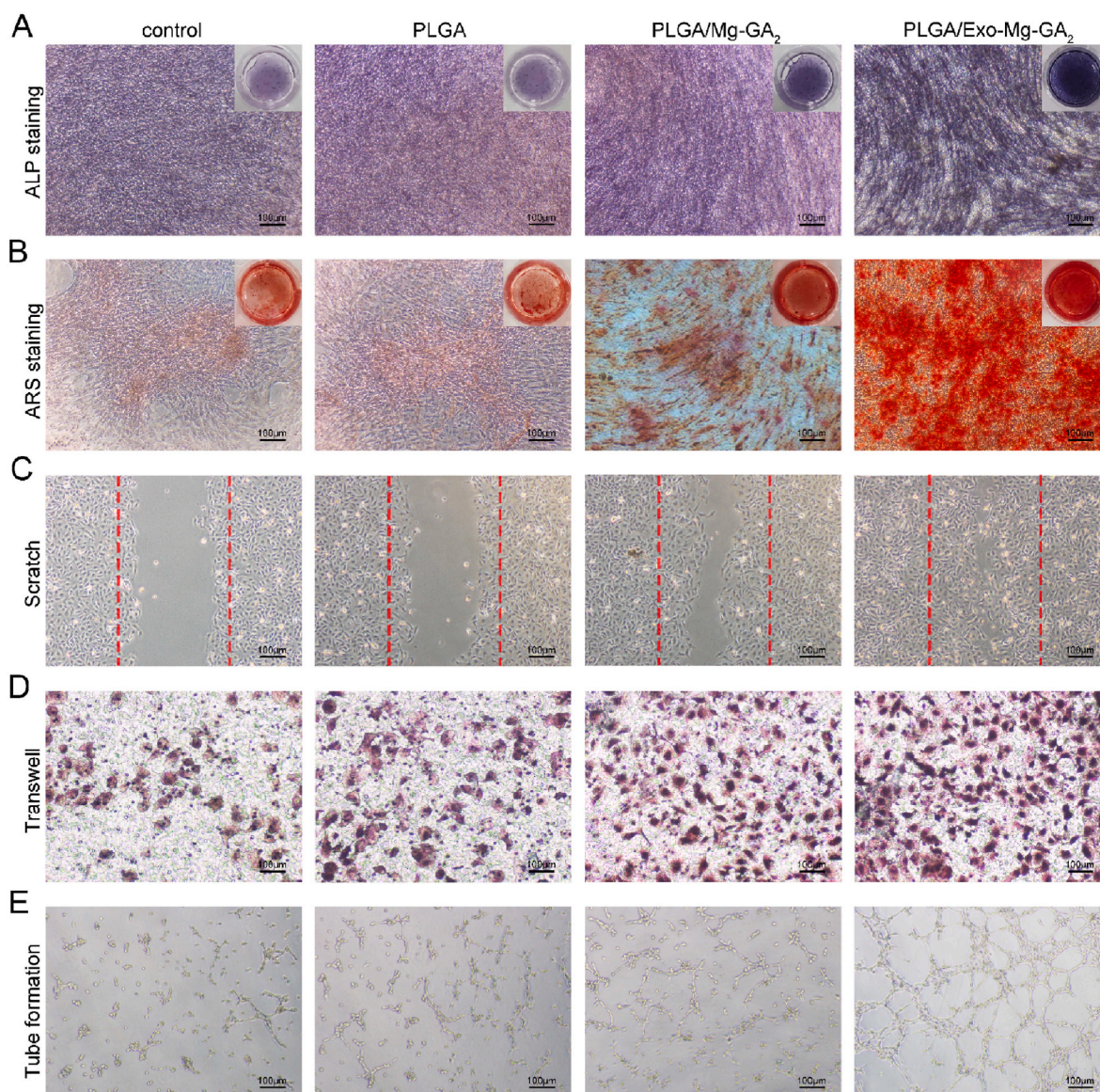
Fig. 6. *In vitro* **osteogenic and angiogenic effects of the extracts from different scaffolds.** **(A)** ALP staining of hBMSCs in the extracts. **(B)** ARS staining of hBMSCs in the extracts. **(C)** Representative images of wound healing assay at 24 h. **(D)** Representative images of transwell assay at 24 h. **(E)** Representative images of tube formation assay at 6 h.

easily and adhere to scaffold surfaces [54,55]. Our data were consistent with these reports. Thus, we theorized that the slow release of Mg^{2+} and GA, the large surface area of Mg-GA MOF, and the specific Mg-GA MOF nanostructure contributed to these results. Importantly, the PLGA/Mg-GA$_2$ group showed the most effective osteogenic ability when compared with other groups, therefore it was used in subsequent experiments.

3.5. Human ADSCs-Exos adhesion to PLGA/Mg-GA MOF scaffolds

The average zeta potential of exosomes was - 30.7 ± 1.1 mV, and the average zeta potential of Mg-GA MOF was +10.9 ± 0.5 mV (Fig. 4A). Mg-GA MOF electrospun fibers were positively charged and enabled the tethering of hADSCs-Exos to Mg-GA MOF surfaces due to the negative potential of exosome membranes (Fig. 4E). And then we set up three mixing ratios of different concentrations (exosome: Mg-GA = 0.75, 1, 1.25) according to the three different PLGA/Exo-Mg-GA MOF scaffolds (Fig. S8). And then we measured the potential of the mixing. With the gradual increase of Mg-GA MOF addition, the zeta potential changed

from negative to positive. Self-assembly of the exosomes and Mg-GA MOF was driven by electrostatic interactions between the negatively charged exosomes and the positively charged Mg-GA MOF (Fig. 4A). Furthermore, some previous studies have demonstrated the existence of electrostatic interactions between exosomes and MOF materials [56,57]. Additionally, some specific interactions (e.g., electrostatic, hydrophilic, and coordination) between the membrane of exosome and MOF matrix particles could contribute to the successful preparation of composite nanoparticles [58]. The surface area of Mg-GA MOF and Exo-Mg-GA were 229.4 m^{2}g^{-1} and 154.5 m^{2}g^{-1}, respectively, determined by Brunauer-Emmett-Teller (BET) measurement (Fig. 4B). When exosome-coated Mg-GA MOF, the surface area was reduced. At the same time, it could be clearly seen that the average pore size and pore volume were also decreasing (Table S3). The main reason for this phenomenon may be due to the interaction between exosomes and Mg-GA MOF, which also further demonstrated the successful coating of exosomes onto the surface of MOF. The obviously higher graft efficiency of exosomes was observed in the PLGA/Exo-Mg-GA$_2$ compared with the control (PLGA) group (Fig. 4C). As indicated (Fig. 4D), SEM showed nanoscale
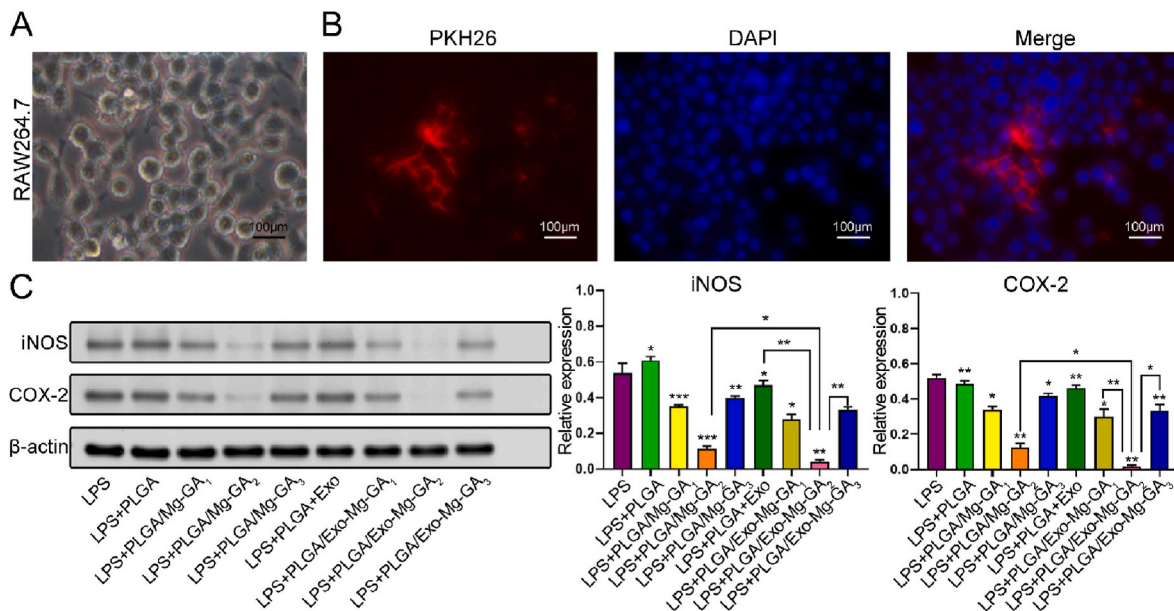
Fig. 7. The anti-inflammatory abilities of exosome-coated Mg-GA MOF scaffolds. (A) Representative photomicrographs of RAW264.7 morphological characteristics. **(B)** Cellular uptake assays show PKH26-labeled exosomes were internalized and distributed in RAW264.7 perinuclear regions. Nuclei were stained with DAPI (blue) and exosomes stained with PKH26 (red). **(C)** Western blot analysis of iNOS and COX-2 expression in RAW264.7 cells cultured on composite scaffolds for 3 days. Lipopolysaccharide (LPS) served as a positive control. Error bars represent standard deviation (SD) from the mean (n = 3) (***$p < 0.001$; **$p < 0.01$; *$p < 0.05$).

roughness on the PLGA/Exo-Mg-GA$_2$ surface due to exosomal coating. In addition, the accumulative release of exosomes from scaffolds was measured using micro-BCA protein assay to confirm the distribution of exosomes in cultured media, which measured at 1 day, 4 days, 7 days, 10 days and 13 days of incubation. Coating exosomes exhibited a continuous and slow release from PLGA/Mg-GA$_2$ scaffolds for up to 10 days (Fig. 4H). These results demonstrated PLGA/Exo-Mg-GA$_2$ scaffolds were suitable for stable and sustained exosome release.

Released exosomes are likely to interact with hBMSCs and HUVECs. To evaluate the impact of exosome-coating on hBMSCs and HUVECs, exosomes were labeled with PKH26, an exosome labeling marker, and incubated with hBMSCs or HUVECs for 12 h. Cellular uptake assays showed that PKH26-labeled exosomes were internalized and distributed in the perinuclear region of hBMSCs and HUVECs (Fig. 4F and G). A recent study showed that exosome-coating of biomaterials accelerated hBMSC cell adhesion, proliferation, osteogenic differentiation [59], and also the transport of numerous pro-angiogenic biomolecules, such as the vascular endothelial growth factor (VEGF) [60,61]. VEGF is crucial for remodeling the vasculature in several regeneration tissues [62,63]. In addition, VEGF expression in hBMSCs is also associated with neo-vascularization [64].

3.6. In vitro biological properties of exosome-coated PLGA/Mg-GA MOF scaffolds

3.6.1. Biocompatibility of exosome-coated PLGA/Mg-GA MOF scaffolds

To investigate the effects of exosome-coated Mg-GA MOF scaffolds on hBMSCs, we explored cell adhesion, proliferation, and osteogenic and angiogenic protein expression of hBMSCs when cultured on PLGA, PLGA/Mg-GA$_2$, and PLGA/Exo-Mg-GA$_2$ scaffolds.

After 72 h, hBMSC morphology on the PLGA/Exo-Mg-GA$_2$ scaffold was spread widely, displaying visible actin filaments with angular structures, and laterally spreading with distinct cytoplasmic extensions (Fig. 5A). The proliferation rate of hBMSCs was higher on PLGA/Exo-Mg-GA$_2$ than PLGA/Mg-GA$_2$ scaffolds, at every time-point (Fig. 5B). Viability observations suggested no cytotoxic effects were generated by scaffolds, with only a few dead cells detected on surfaces (Fig. S9). These

results indicated that hADSCs-Exos on scaffolds interacted with hBMSCs to rapidly promote cell proliferation and adhesion.

3.6.2. Angiogenic and osteogenic properties of exosome-coated PLGA/Mg-GA MOF scaffolds

Because angiogenesis and osteogenesis are intimately linked, we evaluated if the PLGA/Exo-Mg-GA$_2$ scaffold enhances angiogenic and osteogenic protein marker expression. Human BMSCs were collected at indicated time points and subjected to western blotting. As shown (Fig. 5C), when compared with hBMSCs on PLGA/Mg-GA$_2$, cells on PLGA/Exo-Mg-GA$_2$ showed increased expression of ALP, Runx2, OCN, and VEGF after culturing 14 days. Immunofluorescence staining of composite scaffolds further supported our western blotting data (Fig. 5D).

Furthermore, we collected the extracts of the PLGA, PLGA/Mg-GA$_2$, and PLGA/Exo-Mg-GA$_2$. We observed osteogenic differentiation with ALP and ARS staining in hBMSCs. And we measured the functions of wound healing, migration and tube formation in HUVECs. As shown in Fig. 6A, the highest ALP expression was detected in the PLGA/Exo-Mg-GA$_2$ group, followed by the PLGA/Mg-GA$_2$, control and PLGA group. Similar to the trend of ALP staining, ARS staining revealed that the PLGA/Exo-Mg-GA$_2$ group significantly increased the mineralized nodules formation of hBMSCs when compared to the other three groups (Fig. 6B). The wound healing and migration capabilities of HUVECs in the PLGA/Exo-Mg-GA$_2$ group were evidently stronger than those in the other groups. Additionally, HUVECs in the PLGA group or the control group had weakened wound healing and migration capabilities compared with the PLGA/Mg-GA$_2$ group (Fig. 6C and D). The tube formation rate of HUVECs in the PLGA/Exo-Mg-GA$_2$ group was higher than that in the PLGA/Mg-GA$_2$ group. Moreover, the tube formation rate of HUVECs in the PLGA/Mg-GA$_2$ group was higher than that in the control group (Fig. 6E). Thus, exosome coating stimulated both osteogenesis and angiogenesis. Several studies reported that exosome function was largely due to cellular mediated communications by messenger RNAs (mRNAs), microRNAs (miRNAs), and proteins, which then functioned via complex mechanisms to alter target cell activity [65]. For example, exosomes promoted hBMSC osteogenic differentiation through
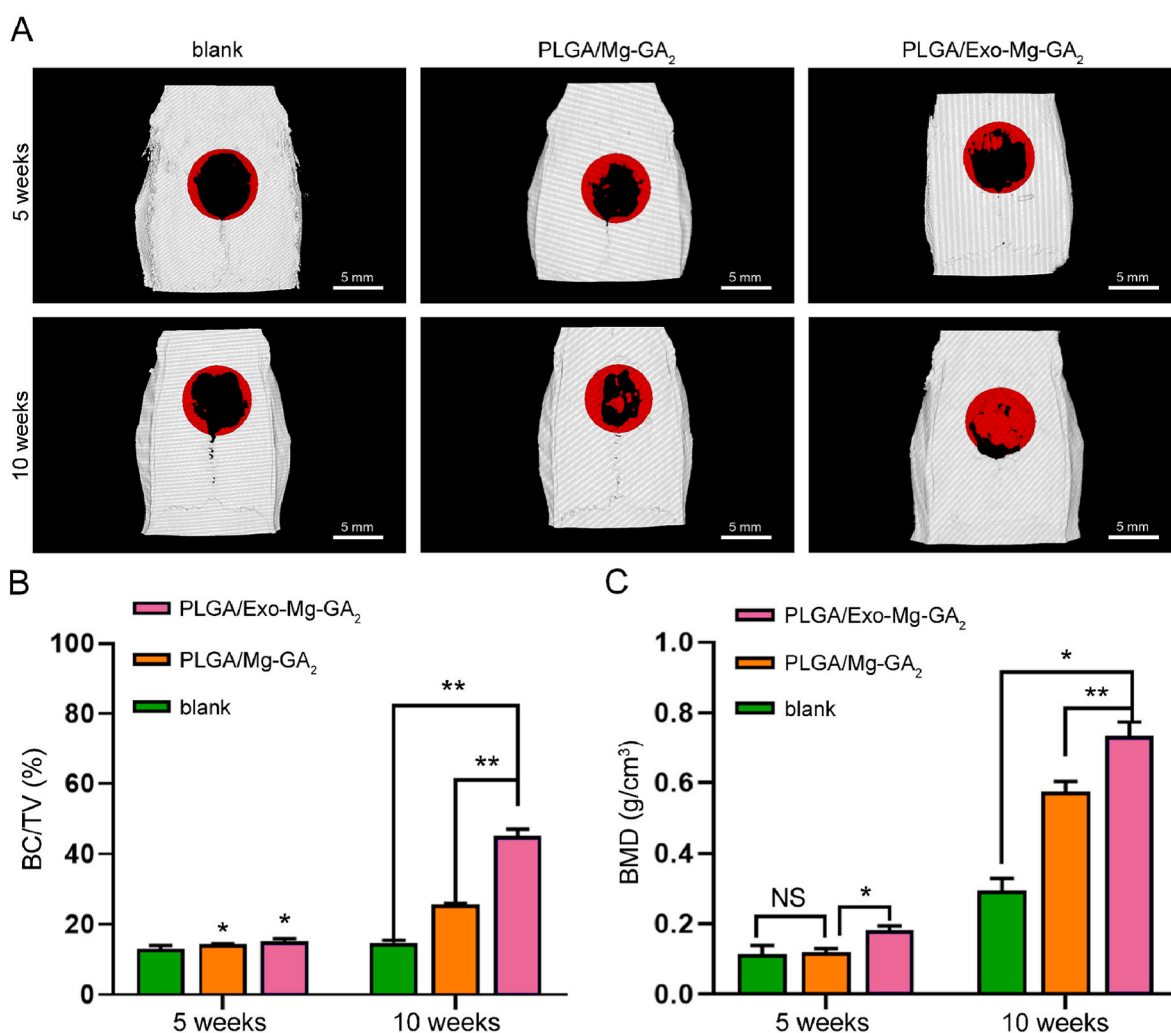
Fig. 8. Micro-computed tomography (CT) was used to evaluate the effects of exosome-coated Mg-GA MOF scaffolds on *in vivo* bone regeneration. (A) Three dimensional (3D) micro-CT images of rat calvarial defect areas implanted with PLGA/Mg-GA$_2$ and PLGA/Exo-Mg-GA$_2$ scaffolds. **(B)** BV/TV ratio of composite scaffolds at 5 weeks and 10 weeks post-surgery. **(C)** BMD ratio of composite scaffolds at 5 weeks and 10 weeks post-surgery. Data are presented as mean ± SD (*$P <$ 0.05, **$P <$ 0.01).

exosomal miR-375 [66]. Similarly, Zhang et al. reported that exosomes were crucial not only for cell-to-cell communications, but also for metabolic and cellular processes, and the regulation of biological processes [67].

3.7. Anti-inflammatory abilities of exosome-coated PLGA/Mg-GA MOF scaffolds

Biomaterial implantation elicits considerable inflammatory responses via pro-inflammatory cytokine release [68]. Prolonged exposure to these molecules eventually culminates in chronic inflammation which induces fibrous encapsulation formation around the implantation material, and finally osseointegration failure [69]. The local release of anti-inflammatory drugs, such as corticosteroids and prostaglandins, can ameliorate inflammatory responses toward implanted biomaterials, however, various side effects, such as cardiotoxicity, hepatotoxicity, and immunological dysfunction can occur over long-term use [70]. Thus, natural, alternative anti-inflammatory drugs have gained considerable traction in the literature; Tanaka et al. reported that GA attenuated LPS-induced inflammatory mediator expression and reactive oxygen species production in RAW264.7 macrophages [71]. Furthermore, growing evidence also suggests that MSC-derived exosomes and Mg^{2+} play roles in inhibiting inflammation [72]. Several studies reported that

MSC-derived exosomes efficiently suppressed detrimental immune response in inflamed tissues, and promoted the survival and regeneration of injured cells [73–75].

In our study, inflammatory responses were evaluated using RAW264.7 cells (Fig. 7A). Thus, exosomes were labeled with PKH26 and incubated with RAW264.7 cells for 12 h. Cellular uptake assays showed that exosomes were internalized and distributed to the perinuclear region of RAW264.7 cells (Fig. 7B). We further characterized the anti-inflammatory effects of Mg^{2+}, GA and exosomes released from scaffolds by assessing iNOS and COX-2 protein levels in RAW264.7 cells grown on scaffold surfaces. All Mg-GA MOF scaffold treated groups demonstrated significantly lower iNOS and COX-2 expression levels than the positive control group when 1 μg/mL LPS was used for inflammation stimulation (Fig. 7C). The PLGA/Mg-GA$_2$ treated group had the lowest iNOS and COX-2 levels when compared with PLGA/Mg-GA$_1$ and PLGA/Mg-GA$_3$ groups, indicating more potent anti-inflammatory abilities. Moreover, exosomes further attenuated LPS-induced inflammatory mediator expression; the PLGA/Exo-Mg-GA$_2$ treated group generated the lowest iNOS and COX-2 expression levels when compared with all other groups. Thus, the PLGA/Exo-Mg-GA$_2$ scaffold effectively suppressed pro-inflammatory mediator expression in LPS-induced RAW264.7 cells, suggesting this scaffold could prevent inflammation. Therefore, the PLGA/Exo-Mg-GA$_2$ was used to create a
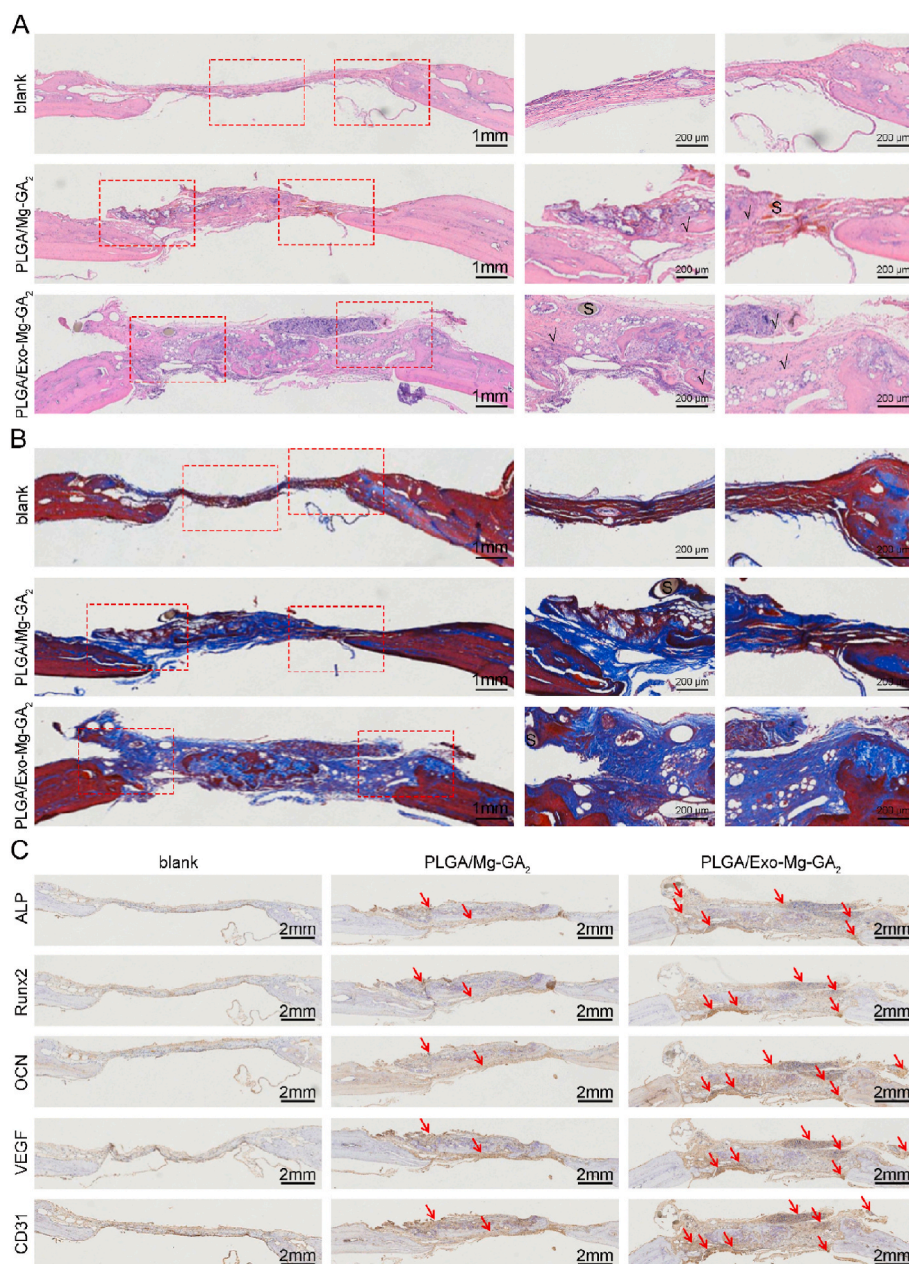
Fig. 9. Histological analysis of exosome-coated Mg-GA MOF scaffolds during *in vivo* treatment. (A) Histological evaluation with HE staining on blank, PLGA/Mg-GA$_2$ and PLGA/Exo-Mg-GA$_2$ scaffold groups at 10 weeks of post-surgery. **(B)** Histological evaluation with MT staining on blank, PLGA/Mg-GA$_2$ and PLGA/Exo-Mg-GA$_2$ scaffold groups at 10 weeks of post-surgery. **(C)** Representative immunohistochemistry images of ALP, Runx2, OCN, CD31, VEGF in different groups (Blank, PLGA/Mg-GA$_2$, PLGA/Exo-Mg-GA$_2$). Red arrows point to the positive staining area. S, scaffold implantant, newly formed bone area marked"√".

bone immune microenvironment around scaffolds to promote interfacial osteogenesis.

3.8. In vivo bone regeneration capacities of exosome-coated Mg-GA MOF scaffolds

Having demonstrated the *in vitro* biological effects of PLGA/Mg-GA$_2$ and PLGA/Exo-Mg-GA$_2$ scaffolds, we next determined the efficacy of both composite scaffolds on osteogenesis, angiogenesis and anti-inflammatory abilities in an *in vivo* rat calvarial defect model.

3.8.1. Micro-computed tomography (CT)

Micro-CT is an excellent method to evaluate bone healing; it is non-invasive and can be used repeatedly to follow time-dependent healing in the same animal. Micro-CT can also be used to measure the volume of newly formed bone, however, it cannot distinguish between fibrous tissue and cartilage [76]. In our study, we observed new bone formation in rat calvarial defects at 5 and 10 weeks after implantation. When

compared to the initial defect size (indicated by the red circle (diameter: 6.5 mm) (Fig. 8A), we observed that the blank, PLGA/Mg-GA$_2$, and PLGA/Exo-Mg-GA$_2$ groups appeared to have weak effects on mineralization at 5 weeks, however, 3D micro-CT images showed greater bone formation and more newly formed calcified bone structures in rats with PLGA/Exo-Mg-GA$_2$ scaffolds at 10 weeks. Interestingly, bone defect healing started from peripheral regions and progressed toward the central area of the defect in the blank group, while PLGA/Mg-GA$_2$ and PLGA/Exo-Mg-GA$_2$ groups showed healing not only from the periphery but also from central regions (Fig. 8A).

Furthermore, we also calculated regenerated volume/total volume (BV/TV) ratios and bone mineral density (BMD) levels using micro-CT results (Fig. 8B and C). The BV/TV ratio at 5 weeks post-surgery in the PLGA/Exo-Mg-GA$_2$ group was 15.167% ± 0.764%, and was slightly higher than the other two groups; 13.033% ± 0.907% and 14.267% ± 0.208%, in the blank and the PLGA/Mg-GA$_2$, respectively. Additionally, the BMD of the defect area measured at 5 weeks post-surgery was 1.5-fold higher in the PLGA/Exo-Mg-GA$_2$ group when compared with the

blank and PLGA/Mg-GA$_2$ groups. This improved healing in cranial bone at 5 weeks indicated an enhanced, early stage bone regeneration process. At 10 weeks post-surgery, the BV/TV ratio and BMD in the PLGA/Exo-Mg-GA$_2$ group was 45.167% $\pm$ 1.96% and 0.733 $\pm$ 0.04 g/cm^3, respectively, and was markedly higher than the PLGA/Mg-GA$_2$ group (BV/TV: 25.7% $\pm$ 0.265%, BMD: 0.573 $\pm$ 0.031 g/cm^3), as well as the BV/TV ratio and BMD in the PLGA/Mg-GA$_2$ group was markedly higher than the blank group (BV/TV: 14.7% $\pm$ 0.781%, BMD: 0.293 $\pm$ 0.035 g/cm^3). Hence, these data indicated the strong potential and excellent osteoconductive capacity of the PLGA/Exo-Mg-GA$_2$ scaffolds to promote new *in vivo* bone growth.

3.8.2. Histological analyses of newly formed bone in defects

At 10 weeks post-surgery, rats were humanely sacrificed and their calvarial bones collected. To visualize bone regeneration in defect areas, samples were cut into sections and stained with hematoxylin-eosin (H&E), Masson's Trichome (MT), ALP, Runx2, OCN, VEGF and CD31 antibodies (Fig. 9). All animals had survived the 10 month study period, and scaffold groups presented no obvious inflammatory cell infiltration at the implantation site, suggesting good scaffold biocompatibility and powerful anti-inflammatory properties of GA and hADSCs-Exos. Mechanistically, GA weakens inflammatory responses by reducing the release of inflammatory cytokines, chemokines, adhesion molecules, and inflammatory cell infiltrates [77]. The anti-inflammatory potential of MSC-Exos was shown to rely on the effects of MSC-sourced bioactive molecules (lipids, enzymes, cytokines, chemokines, immunoregulatory proteins, trophic and growth factors, and microRNAs) which efficiently modulated immune responses and promoted tissue repair and regeneration [78]. At 10 weeks, H&E staining (Fig. 9A) showed that the defect area was covered by bone collagen and new bone tissue in the PLGA/Exo-Mg-GA$_2$ group, while the blank group contained mainly fibroblasts and hyperplastic fibrous tissue. The PLGA/Exo-Mg-GA$_2$ group contained considerably more new bone formation when compared to the PLGA/Mg-GA$_2$ group, and the least amount of bone formation was observed in the blank group. MT staining indicated that more mature collagen fibers were present in the PLGA/Exo-Mg-GA$_2$ group when compared with the other groups (Fig. 9B).

The immunohistochemistry (IHC) staining was performed to detect specific expression patterns of osteogenic and angiogenic proteins, including ALP, Runx2, OCN, VEGF and CD31. As shown (Fig. 9C), all markers in the PLGA/Exo-Mg-GA$_2$ group were highly expressed, followed by the PLGA/Mg-GA$_2$ group, with the blank group displaying the lowest levels. IHC staining of VEGF and CD31 indicated that PLGA/Exo-Mg-GA$_2$ scaffolds may have stimulated the release of Mg^{2+} and exosomes, which contributed to the creation of a pro-angiogenic biochemical microenvironment. Both PLGA/Mg-GA$_2$ and PLGA/Exo-Mg-GA$_2$ scaffold implants showed bone regeneration capacities and biocompatibility after transplantation at injured sites. Collectively, these results were attributed to the collective effects of released Mg^{2+}, GA, and exosomes, and also the specific Mg-GA MOF nanostructure. Similarly, the PLGA/Exo-Mg-GA$_2$ scaffold efficiently promoted bone regeneration when transplanted into a bone defect *in vivo* rat model.

4. Conclusion

Biocompatible PLGA/Mg-GA MOF composite scaffolds were prepared using electrospinning technology. This system generated unique nanostructures and the ability to manipulate the slow release of Mg ions and GA, thereby affecting the osteogenic ability of hBMSCs, angiogenic ability of HUVECs and some anti-inflammation effects in RAW264.7 cells. Human ADSCs-derived Exos were densely and uniformly deposited on PLGA/Mg-GA$_2$ scaffolds and exhibited a continuous slow release for up to 10 days. Slowly released hADSCs-Exos were phagocytosed by co-cultured cells, which stabilized the bone graft environment, ensured a blood supply, promoted osteogenic differentiation, and accelerated bone reconstruction. Both *in vitro* and *in vivo* results revealed that PLGA/Exo-Mg-GA$_2$ effectively increased osteogenesis and angiogenesis, and enhanced anti-inflammatory abilities.

From the above experiment results, we consider that such kind of exosome-coated nanocomposite scaffolds will provide a significant clinical platform technology for bone defect repair.

CRediT authorship contribution statement

Yue Kang: Conceptualization, Methodology, Validation, Investigation, Writing – original draft. **Chang Xu:** Methodology, Formal analysis. **Ling'ao Meng:** Methodology, Validation. **Xufeng Dong:** Writing – review & editing. **Min Qi:** Methodology, Writing – review & editing, Supervision. **Daqing Jiang:** Methodology, Validation, Writing – review & editing, Supervision.

Declaration of competing interest

The authors declare there are no competing interests.

Acknowledgments

Appendix B. Supplementary data

Supplementary data to this article can be found online at https://doi.org/10.1016/j.bioactmat.2022.02.012.

Appendix A. Supplementary data

The following is the Supplementary data to this article:

References

[1] T. Vos, S.S. Lim, C. Abbafati, et al., Global burden of 369 diseases and injuries in 204 countries and territories, 1990–2019: a systematic analysis for the Global Burden of Disease Study 2019, Lancet 396 (10258) (2020) 1204–1222.

[2] W.R. Moore, S.E. Graves, G.I. Bain, Synthetic bone graft substitutes, ANZ J. Surg. 71 (6) (2001) 354–361.

[3] C. Delloye, O. Cornu, V. Druez, et al., Bone allografts: what they can offer and what they cannot, J. Bone Jt. Surg. Br. Vol. 89 (5) (2007) 574–580.

[4] F. Duttenhoefer, R. Lara de Freitas, T. Meury, et al., 3D scaffolds co-seeded with human endothelial progenitor and mesenchymal stem cells: evidence of prevascularisation within 7 days, Eur. Cells Mater. eCM 26 (2013) 64–65.

[5] L. Roseti, V. Parisi, M. Petretta, et al., Scaffolds for bone tissue engineering: state of the art and new perspectives, Mater. Sci. Eng. C 78 (2017) 1246–1262.

[6] Y. Shi, G. Hu, J. Su, et al., Mesenchymal stem cells: a new strategy for immunosuppression and tissue repair, Cell Res. 20 (5) (2010) 510–518.

[7] J. Wang, L. Wang, M. Yang, et al., Untangling the effects of peptide sequences and nanotopographies in a biomimetic niche for directed differentiation of iPSCs by assemblies of genetically engineered viral nanofibers[J], Nano Lett. 14 (12) (2014) 6850–6856.

[8] M.M. Stevens, R.P. Marini, D. Schaefer, et al., In vivo engineering of organs: the bone bioreactor, Proc. Natl. Acad. Sci. Unit. States Am. 102 (32) (2005) 11450–11455.

[9] M. Zhai, Y. Zhu, M. Yang, et al., Human mesenchymal stem cell derived exosomes enhance cell-free bone regeneration by altering their miRNAs profiles, Adv. Sci. 7 (19) (2020) 2001334.

[10] V.B.R. Konala, M.K. Mamidi, R. Bhonde, et al., The current landscape of the mesenchymal stromal cell secretome: a new paradigm for cell-free regeneration, Cytotherapy 18 (1) (2016) 13–24.

[11] J.N. Zara, R.K. Siu, X. Zhang, et al., High doses of bone morphogenetic protein 2 induce structurally abnormal bone and inflammation in vivo, Tissue Eng. 17 (9–10) (2011) 1389–1399.

[12] W. Wang, N. Zhu, T. Yan, et al., The crosstalk: exosomes and lipid metabolism, Cell Commun. Signal. 18 (1) (2020) 1–12.

[13] Q. Li, H. Yu, M. Sun, et al., The tissue origin effect of extracellular vesicles on cartilage and bone regeneration, Acta Biomater. 125 (2021) 253–266.

[14] C.R. Harrell, N. Jovicic, V. Djonov, et al., Mesenchymal stem cell-derived exosomes and other extracellular vesicles as new remedies in the therapy of inflammatory diseases, Cells 8 (12) (2019) 1605.

[15] A. Trzyna, A. Banaś-Ząbczyk, Adipose-derived stem cells secretome and its potential application in "stem cell-free therapy", Biomolecules 11 (6) (2021) 878.

[16] F. Xu, Q. Xiang, J. Huang, et al., Exosomal miR-423-5p mediates the proangiogenic activity of human adipose-derived stem cells by targeting Sufu, Stem Cell Res. Ther. 10 (1) (2019) 1–14.

[17] S. Kholia, A. Ranghino, P. Garnieri, et al., Extracellular vesicles as new players in angiogenesis, Vasc. Pharmacol. 86 (2016) 64–70.

[18] O.M. Yaghi, G. Li, H. Li, Selective binding and removal of guests in a microporous metal-organic framework, Nature 378 (6558) (1995) 703–706.

[19] D. Fairen-Jimenez, S.A. Moggach, M.T. Wharmby, et al., Opening the gate: framework flexibility in ZIF-8 explored by experiments and simulations, J. Am. Chem. Soc. 133 (23) (2011) 8900–8902.

[20] K.K. Tanabe, S.M. Cohen, Engineering a metal-organic framework catalyst by using postsynthetic modification, Angew. Chem. 121 (40) (2009) 7560–7563.

[21] Y. Liu, Z. Zhu, X. Pei, et al., ZIF-8-Modified multifunctional bone-adhesive hydrogels promoting angiogenesis and osteogenesis for bone regeneration, ACS Appl. Mater. Interfaces 12 (33) (2020) 36978–36995.

[22] L. Cooper, T. Hidalgo, M. Gorman, et al., A biocompatible porous Mg-gallate metal-organic framework as an antioxidant carrier, Chem. Commun. 51 (27) (2015) 5848–5851.

[23] K. Glenske, P. Donkiewicz, A. Köwitsch, et al., Applications of metals for bone regeneration, Int. J. Mol. Sci. 19 (3) (2018) 826.

[24] T. Qi, J. Weng, F. Yu, et al., Insights into the role of magnesium ions in affecting osteogenic differentiation of mesenchymal stem cells, Biol. Trace Elem. Res. 199 (2021) 559–567.

[25] S. Yoshizawa, A. Brown, A. Barchowsky, et al., Role of magnesium ions on osteogenic response in bone marrow stromal cells, Connect. Tissue Res. 55 (sup1) (2014) 155–159.

[26] C. Liu, G. Yang, M. Zhou, et al., Magnesium ammonium phosphate composite cell-laden hydrogel promotes osteogenesis and angiogenesis in vitro, ACS Omega 6 (14) (2021) 9449–9459.

[27] Z. Lin, D. Shen, W. Zhou, et al., Regulation of extracellular bioactive cations in bone tissue microenvironment induces favorable osteoimmune conditions to accelerate in situ bone regeneration, Bioact. Mater. 6 (8) (2021) 2315–2330.

[28] J. Bai, Y. Zhang, C. Tang, et al., Gallic acid: pharmacological activities and molecular mechanisms involved in inflammation-related diseases, Biomed. Pharmacother. 133 (2021) 110985.

[29] J.M. Sadowska, M.P. Ginebra, Inflammation and biomaterials: role of the immune response in bone regeneration by inorganic scaffolds, J. Mater. Chem. B 8 (41) (2020) 9404–9427.

[30] J. Zhuang, C.H. Kuo, L.Y. Chou, et al., Optimized metal–organic-framework nanospheres for drug delivery: evaluation of small-molecule encapsulation, ACS Nano 8 (3) (2014) 2812–2819.

[31] W.H. Chen, G.F. Luo, M. Vazquez-Gonzalez, et al., Glucose-responsive metal-organic-framework nanoparticles act as "smart" sense-and-treat carriers, ACS Nano 12 (8) (2018) 7538–7545.

[32] M. Xu, Y. Hu, W. Ding, et al., Rationally designed rapamycin-encapsulated ZIF-8 nanosystem for overcoming chemotherapy resistance, Biomaterials 258 (2020) 120308.

[33] K.K. Chereddy, G. Vandermeulen, V. Préat, PLGA based drug delivery systems: promising carriers for wound healing activity, Wound Repair Regen. 24 (2) (2016) 223–236.

[34] X. Zhou, Z. Wang, Y.K. Chan, et al., Infection micromilieu-activated nanocatalytic membrane for orchestrating rapid sterilization and stalled chronic wound regeneration, Adv. Funct. Mater. (2021) 2109469.

[35] A.O. Pereira, I.M.I. Lopes, T.R. Silva, et al., Bacterial photoinactivation using PLGA electrospun scaffolds, ACS Appl. Mater. Interfaces 13 (27) (2021) 31406–31417.

[36] Y. Kang, S. Guo, Q. Sun, T. Zhang, J. Liu, D. He, Differential circular RNA expression profiling during osteogenic differentiation in human adipose-derived stem cells, Epigenomics 12 (4) (2020 Feb) 289–302.

[37] T. Mukhiya, A. Muthurasu, A.P. Tiwari, et al., Integrating the essence of a metal-organic framework with electrospinning: a new approach for making a metal nanoparticle confined N-doped carbon nanotubes/porous carbon nanofibrous membrane for energy storage and conversion, ACS Appl. Mater. Interfaces 13 (20) (2021) 23732–23742.

[38] J. Zhang, Y. Liu, Y. Chen, et al., Adipose-derived stem cells: current applications and future directions in the regeneration of multiple tissues, Stem Cell. Int. (2020 Dec 10) 8810813.

[39] P.A. Zuk, M.I.N. Zhu, H. Mizuno, et al., Multilineage cells from human adipose tissue: implications for cell-based therapies, Tissue Eng. 7 (2) (2001) 211–228.

[40] B.A. Bunnell, M. Flaat, C. Gagliardi, et al., Adipose-derived stem cells: isolation, expansion and differentiation, Methods 45 (2) (2008) 115–120.

[41] X.F. Yang, X. He, J. He, et al., High efficient isolation and systematic identification of human adipose-derived mesenchymal stem cells, J. Biomed. Sci. 18 (1) (2011) 1–9.

[42] Z. Zheng, Y. Chen, B. Guo, et al., Magnesium-organic framework-based stimuli-responsive systems that optimize the bone microenvironment for enhanced bone regeneration, Chem. Eng. J. 396 (2020) 125241.

[43] M. Yin, W. Wu, M. Deng, et al., Multifunctional magnesium organic framework-based microneedle patch for accelerating diabetic wound healing, ACS Nano 15 (11) (2021) 17842–17853.

[44] M. Bongio, J.J.J.P. Van Den Beucken, S.C.G. Leeuwenburgh, et al., Development of bone substitute materials: from 'biocompatible' to 'instructive', J. Mater. Chem. 20 (40) (2010) 8747–8759.

[45] S.S. Lee, M. Santschi, S.J. Ferguson, A biomimetic macroporous hybrid scaffold with sustained drug delivery for enhanced bone regeneration, Biomacromolecules (2021).

[46] S. Wang, F. Hu, J. Li, et al., Design of electrospun nanofibrous mats for osteogenic differentiation of mesenchymal stem cells, Nanomed. Nanotechnol. Biol. Med. 14 (7) (2018) 2505–2520.

[47] L. Li, M. Yu, Y. Li, et al., Synergistic anti-inflammatory and osteogenic n-HA/resveratrol/chitosan composite microspheres for osteoporotic bone regeneration, Bioact. Mater. 6 (5) (2021) 1255–1266.

[48] A.R. Bastos, F.R. Maia, J.M. Oliveira, et al., Influence of gellan gum-hydroxyapatite spongy-like hydrogels on human osteoblasts under long-term osteogenic differentiation conditions, Mater. Sci. Eng. C 129 (2021) 112413.

[49] T. Nakamura, A. Nakamura-Takahashi, M. Kasahara, et al., Tissue-nonspecific alkaline phosphatase promotes the osteogenic differentiation of osteoprogenitor cells, Biochem. Biophys. Res. Commun. 524 (3) (2020) 702–709.

[50] M. Chen, Q. Liu, Y. Xu, et al., The effect of LyPRP/collagen composite hydrogel on osteogenic differentiation of rBMSCs, Regen. Biomater. 8 (1) (2021) rbaa053.

[51] X. Li, M. Wang, W. Zhang, et al., A magnesium-incorporated nanoporous titanium coating for rapid osseointegration, Int. J. Nanomed. 15 (2020) 6593.

[52] Z. Wu, Z. Meng, Q. Wu, et al., Biomimetic and osteogenic 3D silk fibroin composite scaffolds with nano MgO and mineralized hydroxyapatite for bone regeneration, J. Tissue Eng. 11 (2020), 2041731420967791.

[53] Y. Oh, C.B. Ahn, M. Marasinghe, et al., Insertion of gallic acid onto chitosan promotes the differentiation of osteoblasts from murine bone marrow-derived mesenchymal stem cells, Int. J. Biol. Macromol. 183 (2021) 1410–1418.

[54] Y. Xia, X. Fan, H. Yang, et al., ZnO/Nanocarbons-Modified fibrous scaffolds for stem cell-based osteogenic differentiation, Small 16 (38) (2020) 2003010.

[55] Y.A. Petrenko, R.V. Ivanov, A.Y. Petrenko, et al., Coupling of gelatin to inner surfaces of pore walls in spongy alginate-based scaffolds facilitates the adhesion, growth and differentiation of human bone marrow mesenchymal stromal cells, J. Mater. Sci. Mater. Med. 22 (6) (2011) 1529–1540.

[56] B. Illes, P. Hirschle, S. Barnert, et al., Exosome-coated metal–organic framework nanoparticles: an efficient drug delivery platform, Chem. Mater. 29 (19) (2017) 8042–8046.

[57] N. Zhang, N. Sun, C. Deng, A hydrophilic magnetic MOF for the consecutive enrichment of exosomes and exosomal phosphopeptides, Chem. Commun. 56 (90) (2020) 13999–14002.

[58] G. Cheng, W. Li, L. Ha, et al., Self-assembly of extracellular vesicle-like metal–organic framework nanoparticles for protection and intracellular delivery of biofunctional proteins, J. Am. Chem. Soc. 140 (23) (2018) 7282–7291.

[59] D.K. Kim, S. Lee, M. Kim, et al., Exosome-coated silk fibroin 3D-scaffold for inducing osteogenic differentiation of bone marrow derived mesenchymal stem cells, Chem. Eng. J. 406 (2021) 127080.

[60] Y. Han, J. Ren, Y. Bai, et al., Exosomes from hypoxia-treated human adipose-derived mesenchymal stem cells enhance angiogenesis through VEGF/VEGF-R, Int. J. Biochem. Cell Biol. 109 (2019) 59–68.

[61] P. Hong, H. Yang, Y. Wu, et al., The functions and clinical application potential of exosomes derived from adipose mesenchymal stem cells: a comprehensive review, Stem Cell Res. Ther. 10 (1) (2019) 1–12.

[62] M.M. Martino, F. Tortelli, M. Mochizuki, et al., Engineering the growth factor microenvironment with fibronectin domains to promote wound and bone tissue healing, Sci. Transl. Med. 3 (100) (2011), 100ra89-100ra89.

[63] D.H. Choi, R. Subbiah, I.H. Kim, et al., Dual growth factor delivery using biocompatible core–shell microcapsules for angiogenesis, Small 9 (20) (2013) 3468–3476.

[64] W. Fan, R. Crawford, Y. Xiao, The ratio of VEGF/PEDF expression in bone marrow mesenchymal stem cells regulates neovascularization, Differentiation 81 (3) (2011) 181–191.

[65] F. Urabe, Y. Yoshioka, T. Ochiya, The biological role of exosomes in bone remodeling and bone diseases, Clin. Calcium 28 (1) (2018) 122–127.

[66] S. Chen, Y. Tang, Y. Liu, et al., Exosomes derived from miR-375-overexpressing human adipose mesenchymal stem cells promote bone regeneration, Cell Prolif 52 (5) (2019), e12669.

[67] Y. Zhang, Y. Liu, H. Liu, et al., Exosomes: biogenesis, biologic function and clinical potential, Cell Biosci. 9 (1) (2019) 1–18.

[68] M. He, B. Yang, F. Huo, et al., A novel Coating with universal adhesion and inflammation-responsive drug release functions to manipulate osteoimmunomodulation of implants, J. Mater. Chem. B (2021).

[69] L. Fan, P. Guan, C. Xiao, et al., Exosome-functionalized polyetheretherketone-based implant with immunomodulatory property for enhancing osseointegration, Bioact. Mater. 6 (9) (2021) 2754–2766.

[70] Y.H. Wang, K.W. Zeng, Natural products as a crucial source of anti-inflammatory drugs: recent trends and advancements, Trad. Med. Res. 4 (5) (2019) 257–268.

[71] M. Tanaka, Y. Kishimoto, M. Sasaki, et al., Terminalia bellirica (gaertn.) roxb. Extract and gallic acid attenuate LPS-induced inflammation and oxidative stress via MAPK/NF-κB and Akt/AMPK/Nrf2 pathways, Oxidat. Med. Cell. Longev. (2018).

[72] B. Li, P. Gao, H. Zhang, et al., Osteoimmunomodulation, osseointegration, and in vivo mechanical integrity of pure Mg coated with HA nanorod/pore-sealed MgO bilayer, Biomater. Sci. 6 (12) (2018) 3202–3218.

[73] C.R. Harrell, R. Sadikot, J. Pascual, et al., Mesenchymal stem cell-based therapy of inflammatory lung diseases: current understanding and future perspectives, Stem Cells Int. (2019).

[74] G. Sun, G. Li, D. Li, et al., hucMSC derived exosomes promote functional recovery in spinal cord injury mice via attenuating inflammation, Mater. Sci. Eng. C 89 (2018) 194–204.

[75] Z. Julier, A.J. Park, P.S. Briquez, et al., Promoting tissue regeneration by modulating the immune system, Acta Biomater. 53 (2017) 13–28.

[76] Z. Han, M. Bhavsar, L. Leppik, et al., Histological scoring method to assess bone healing in critical size bone defect models, Tissue Eng. C Methods 24 (5) (2018) 272–279.

[77] S.H. Kim, C.D. Jun, K. Suk, et al., Gallic acid inhibits histamine release and pro-inflammatory cytokine production in mast cells, Toxicol. Sci. 91 (1) (2006) 123–131.

[78] D.G. Phinney, M.F. Pittenger, Concise review: MSC-derived exosomes for cell-free therapy, Stem Cell. 35 (4) (2017) 851–858.